Variability in sulfur isotope records of Phanerozoic seawater sulfate

Theodore Michael Present[1,1], Jess Adkins[1,1], and Woodward Fischer[1,1]

[1]California Institute of Technology

November 30, 2022

Abstract

The δ34S of seawater sulfate reflects processes operating at the nexus of sulfur, carbon, and oxygen cycles. However, knowledge of past seawater sulfate δ34S values must be derived from proxy materials that are impacted differently by depositional and post-depositional processes. We produced new timeseries estimates for the δ34S value of seawater sulfate by combining 6710 published data from three sedimentary archives—marine barite, evaporites, and carbonate-associated sulfate—with updated age constraints on the deposits. Robust features in multiple records capture temporal trends in the δ34S value of seawater and its interplay with other Phanerozoic geochemical and stratigraphic trends. However, high-frequency discordances indicate that each record is differentially prone to depositional biases and diagenetic overprints. The amount of noise, quantified from the variograms of each record, increases with age for all δ34S proxies, indicating that post-depositional processes obscure detailed knowledge of seawater sulfate's δ34S value deeper in time.

VARIABILITY IN SULFUR ISOTOPE RECORDS OF PHANEROZOIC SEAWATER SULFATE

Theodore M. Present[1], Jess F. Adkins[1], and Woodward W. Fischer[1]

[1]California Institute of Technology, Pasadena, California, USA

Corresponding author: Theodore M. Present (ted@caltech.edu)

Key Points

- 6710 measurements of $\delta^{34}S$ of sulfate in Phanerozoic sedimentary rocks were compiled and systematically updated to a consistent time scale
- Records derived from evaporites, barite, and carbonate-associated sulfate are similar, but also contain dramatic short-term discrepancies
- Variation created by diagenetic and depositional processes increases with age in all records, obscuring temporal trends in marine sulfate

Plain Language Summary

Sedimentary rocks deposited in ancient marine basins preserve a record of seawater composition. We compare the sulfur isotopic composition of three sedimentary materials that contain sulfate—a major ion in seawater important for carbon and oxygen cycling. Evaporite salts, the mineral barite, and trace sulfate in limestone each reveal the same first-order trends over the last 541 million years, but also display substantial shorter order discrepancies that reflect how the materials capture and store paleooceanographic information. These discrepancies partially obscure understanding of the relationship between life, ocean chemistry, and climate.

Keywords

Phanerozoic seawater composition; marine sulfate proxies; carbonate-associated sulfate; evaporites; barite; sulfur isotope ratios; kriging

Abstract

The $\delta^{34}S$ of seawater sulfate reflects processes operating at the nexus of sulfur, carbon, and oxygen cycles. However, knowledge of past seawater sulfate $\delta^{34}S$ values must be derived from proxy materials that are impacted differently by depositional and post-depositional processes. We produced new timeseries estimates for the $\delta^{34}S$ value of seawater sulfate by combining 6710 published data from three sedimentary archives—marine barite, evaporites, and carbonate-associated sulfate—with updated age constraints on the deposits. Robust features in multiple records capture temporal trends in the $\delta^{34}S$ value of seawater and its interplay with other Phanerozoic geochemical and stratigraphic trends. However, high-frequency discordances indicate that each record is differentially prone to depositional biases and diagenetic overprints. The amount of noise, quantified from the variograms of each record, increases with age for all $\delta^{34}S$ proxies, indicating that post-depositional processes obscure detailed knowledge of seawater sulfate's $\delta^{34}S$ value deeper in time.

1 Introduction

Seawater sulfate acts as a major oxidant of organic carbon, controlling the cadence of its burial in sediments and connecting the carbon, sulfur, and oxygen cycles (Bowles et al., 2014; Jørgensen, 1982). Microbial sulfate reduction (MSR), reoxidation of sulfide, and the burial and oxidation of pyrite govern sedimentary inorganic carbon and alkalinity fluxes (Ben-Yaakov, 1973; Froelich et al., 1979). Pyrite in sedimentary rocks may be exposed and oxidized during uplift, erosion, and weathering—impacting Earth's dioxygen and carbon dioxide budgets on tectonic timescales (Burke et al., 2018; Kump & Garrels, 1986; M. A. Torres et al., 2014). Over Phanerozoic time (the past 541 Myr), the burial of sulfide and disulfide minerals must have balanced the acid produced and dioxygen consumed during terrestrial pyrite weathering. Therefore, tracking ancient sulfate fluxes related to these processes illuminates when, how, and where the Earth system achieves this balance, and what happens during intervals of unsteadiness.

Thode et al. (1953) first recognized that a record of ancient marine sulfur isotopic compositions ($\delta^{34}S$) could constrain changes to Earth's biogeochemical cycles, and Ault and Kulp (1959) applied mass balance assumptions in an early effort to quantify important sulfur fluxes. Isotope fractionations during MSR preferentially enrich the residual sulfate in ^{34}S by several percent (Bradley et al., 2016; Harrison & Thode, 1958; Sim et al., 2011). When more sulfate is reduced and fixed into pyrite, removing more light sulfur isotopes from the oceans, the remaining sulfate in seawater becomes enriched in the heavy, rare isotopes. Holland (1973) first attempted to calculate changes in dioxygen fluxes from $\delta^{34}S$ data. Holser (1977) further recognized that rapid changes in the $\delta^{34}S$ value of seawater coincide with intervals of biotic crises and dramatic reorganizations of Earth's climate and biosphere. The subsequent forty years have seen many efforts to derive an accurate and precise record of how the $\delta^{34}S$ value of seawater sulfate has changed over Earth history.

Three sedimentary materials constitute proxy archives of Phanerozoic seawater sulfate $\delta^{34}S$ values: (1) marine evaporites, which include sulfate salts precipitated from evaporated seawater in marginal marine basins; (2) marine barite, which forms from a suite of biogeochemical processes associated with sinking particles in pelagic waters; and (3) carbonate-associated sulfate (CAS), which is minor sulfate incorporated into the crystal lattice of biogenic and abiogenic calcite, aragonite, and dolomite phases that accumulate in sedimentary rocks.

Important reviews (Bottrell & Newton, 2006; Claypool et al., 1980; Holser et al., 1989; Strauss, 1997; Veizer et al., 1980) on the evolution of the Phanerozoic sulfur cycle have assumed that these proxies more-or-less accurately preserve the isotopic composition of ancient seawater sulfate. This assumption is reasonable because Phanerozoic seawater likely contained abundant sulfate as a conservative, well-mixed anion. Modern seawater has 28 mmol/kg sulfate, which has an approximate residence time of more than 10 Myr—much longer than the mixing time of the oceans (Bottrell & Newton, 2006; Walker, 1986). Supergiant gypsum and anhydrite deposits in the sedimentary record indicate that sulfate has been a major constituent in ancient seawater, as well. These deposits, which represent long-lived intervals of basin recharge and evaporation of seawater (Warren, 2010), formed episodically from Mesoproterozoic through Phanerozoic time (Grotzinger & Kasting, 1993; Pope & Grotzinger, 2003). The composition of fluid inclusions in halite from evaporite deposits further suggested that sulfate maintained at least millimolar concentrations throughout Phanerozoic time (Lowenstein et al., 2003).

Important features in the $\delta^{34}S$ age curves were observed in multiple datasets on both long and short timescales. All archives exhibited high $\delta^{34}S$ values in early Paleozoic time, fell to minima in the late Paleozoic, and increased to modern values (~21‰) over Mesozoic and Cenozoic time. This pattern was originally noted in the evaporite record by Ault and Kulp (1959) and reaffirmed by more extensive evaporite compilations (Claypool et al., 1980; Holser et al., 1989; Holser & Kaplan, 1966; Strauss, 1997). Burdett et al. (1989) produced the first continuous biogenic CAS dataset for the Neogene Period and demonstrated that it agreed with the evaporite $\delta^{34}S$ record. Kampschulte et al. (2001) and Kampschulte and Strauss (2004) then demonstrated that biogenic CAS captured the first-order features of the Phanerozoic evaporite record, and could be correlated with higher resolution and confidence than evaporites to the carbonate carbon isotope record. The $\delta^{34}S$ pattern covaries with many other geochemical records of changing seawater composition (Hannisdal & Peters, 2011; Prokoph et al., 2008), and so has been interpreted to reflect long-term changes related to the assembly and breakup of Pangea (Turchyn & DePaolo, 2019).

In addition to long-term trends, Holser (1977) identified shorter fluctuations (5–50 Myr) in the Upper Devonian and lower Triassic evaporite record; these excursions are recorded by CAS as well (Kampschulte & Strauss, 2004). Increased temporal resolution from barite and CAS found additional rapid excursions, notably associated with Jurassic and Cretaceous intervals of widespread organic-rich shale deposition (Gill, Lyons, & Jenkyns, 2011; Paytan et al., 2004) and Paleogene carbon cycle perturbation (Paytan et al., 1998; Rennie et al.,

2018). In addition, some $\delta^{34}S$ records with high temporal resolution, especially derived from CAS, have rapid variability (Kah et al., 2016; Kampschulte et al., 2001), and data from multiple locations containing similar-age strata have $\delta^{34}S$ heterogeneity (Gill, Lyons, Young, et al., 2011; Present et al., 2015).

Although seawater sulfate was likely well-mixed for much of Phanerozoic time, these rapidly varying datasets indicated that short periods of sulfate drawdown may have been expressed as high spatial and temporal $\delta^{34}S$ gradients (Holser, 1977; Kah et al., 2004, 2016). If these gradients represent globally relevant budgets of carbon, nutrients, and oxidizing capacity, then the residence time of sulfate in ancient oceans must have been much shorter than today. An analogy to the carbon cycle is illustrative. Isotopic fractionations between oxidized and reduced species are comparable for carbon and sulfur. The biological pump—remineralization of sinking organic matter that is fractionated by tens of permille from dissolved inorganic carbon—is only capable of creating inorganic carbon isotopic gradients of less than 3‰ given Pliocene-age to present nutrient inventories and *ca.* 2 mmol/kg bicarbonate (Toggweiler & Sarmiento, 1985). Therefore, even small gradients in the $\delta^{34}S$ of marine sulfate, of similar magnitude to carbon isotope gradients driven by the biological pump, would have required both a higher proportion of anaerobic organic carbon remineralization and more than an order of magnitude smaller sulfate inventory.

However, the implicit assumption that proxies for seawater $\delta^{34}S$ values are suitably accurate and precise to demonstrate rapid changes in seawater's composition has not been tested. The processes by which the proxy materials form and incorporate sulfate from seawater may affect their $\delta^{34}S$ value, complicating the reconstruction of Phanerozoic seawater's composition but providing nuance on biogeochemical sulfur cycling and its imprint on the rock record.

We produced a new timeseries to estimate the Phanerozoic history of the $\delta^{34}S$ value of seawater sulfate by synthesizing published geochemical data with updated geochronology and stratigraphic correlations. We attribute some of the differences between archives to mechanics of how sulfate is incorporated into and preserved in sedimentary rocks. This approach tests the assumption that each archive samples the same history of seawater $\delta^{34}S$ values, quantifies uncertainty in proxy archives, and reveals that some major sources of variance are themselves produced by biogeochemical processes that may have varied through Phanerozoic time.

2 Synthesis of Phanerozoic seawater sulfate $\delta^{34}S$ proxy data

We compiled 6710 measurements from 108 references that reported $\delta^{34}S$ values in Phanerozoic marine evaporites, bulk rock CAS, biogenic CAS, or marine barite. Each $\delta^{34}S$ value was assigned an age using the International Commission on Stratigraphy 2016/04 time scale (Cohen et al., 2013; updated) (Figure 1). The Supporting Information enumerates the $\delta^{34}S$ data, assigned age, data type, data source, and method and literature used for each age assignment.

Each proxy material has different, irregularly spaced temporal distributions (Figure 1a). To estimate Phanerozoic $\delta^{34}S$ trends, each proxy record was interpolated at 50 kyr resolution (Figure 1b). Kriging—a geostatistical approach using autocorrelation to quantify stochastic components in spatiotemporal data—was used to weight data for interpolation and estimate confidence intervals (Gebbers, 2010). Because kriging uses the empirical autocorrelation structure of the data to produce weights, it is well suited for irregularly spaced data. Autocorrelation varies between two endmembers of linearly detrended variance: at the maximum is the variance of all points in that geologic interval, and at the minimum is the unresolved chatter between data closely spaced in time. The kriged uncertainty on the interpolations reflects this increase in variance, such that interpolated values further from data have larger uncertainties up to the population variance according to the observed range of autocorrelation. Kriging was done on each geologic material, partitioned by era, by modelling variograms—functions describing how the variance per point (semivariance) of pairs of linearly detrended data varies with their average separation distance in time (Supporting Information). Paleogeography was not considered, so spatial variability was collapsed into the temporally unresolved chatter within each era.

Figure 1 ***[next page]*****.** Records of Phanerozoic seawater sulfate $\delta^{34}S$ generated from proxy materials. **(a)** The average number of $\delta^{34}S$ analyses of each proxy per Myr, in 5 Myr bins, illustrates the temporal bias in the sampling of each material through Phanerozoic time. **(b)** Interpolated proxy records of the $\delta^{34}S$ composition of sulfate over Phanerozoic time. Shading indicates the kriged 1σ confidence intervals. **(c)** All compiled proxy data for the $\delta^{34}S$ of Phanerozoic seawater.

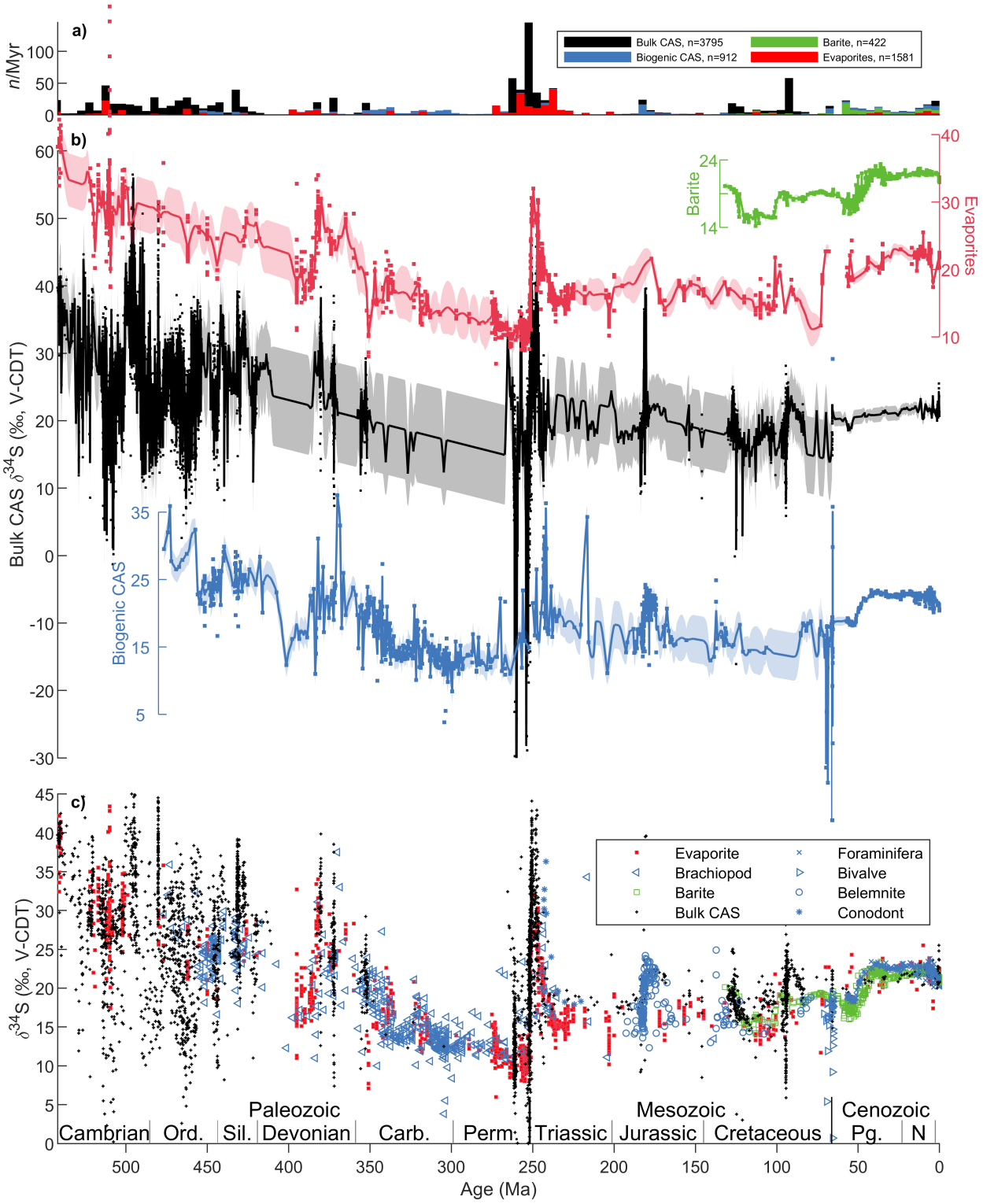
a)
n/Myr
Bulk CAS, n=3795
Biogenic CAS, n=912
Barite, n=422
Evaporites, n=1581
b)
Bulk CAS δ34S (‰, V-CDT)
Biogenic CAS
Barite
Evaporites
c)
δ34S (‰, V-CDT)
Evaporite
Brachiopod
Barite
Bulk CAS
Foraminifera
Bivalve
Belemnite
Conodont
Paleozoic
Mesozoic
Cenozoic
Cambrian
Ord.
Sil.
Devonian
Carb.
Perm.
Triassic
Jurassic
Cretaceous
Pg.
N
Age (Ma)

3 Discussion

3.1 Distribution of $\delta^{34}S$ in proxies

During seventy years of effort to determine a history of Phanerozoic seawater sulfate $\delta^{34}S$ from different geologic materials, it has implicitly been assumed that each proxy samples the same primary population of seawater $\delta^{34}S$ compositions through space and time. However, comparison of all Phanerozoic $\delta^{34}S$ data for each proxy indicates that the four datasets do not come from the same distribution (Supporting Information, non-parametric Kruskal-Wallis one-way analysis of variance, $\chi^2[3,6709] = 684.54$, $p \ll 0.001$). Therefore, each proxy likely has different temporally or spatially variable sampling biases or reflects different biogeochemical processes that contribute to variance in the time-series of ancient sulfate's $\delta^{34}S$.

Major $\delta^{34}S$ trends and excursions in Cenozoic, Mesozoic, and late Paleozoic records are exhibited in multiple archives, but significant discrepancies and gaps are apparent in records from Cambrian to Devonian time (Figure 1c). In early- to mid-Paleozoic strata, biogenic carbonates are sparse, marine barite is absent, and bulk CAS $\delta^{34}S$ values diverge from evaporites by greater than 10‰ (Figure 2a). Additionally, Paleozoic variance is highest for all records (Figure 2b).

The evaporite record, being comprised of massive amounts of sulfate but limited in spatial and temporal extent, likely captures long-term $\delta^{34}S$ trends. The bulk CAS, biogenic CAS, and barite records have higher temporal resolution than the evaporite record for much of the Phanerozoic, potentially capturing shorter $\delta^{34}S$ excursions.

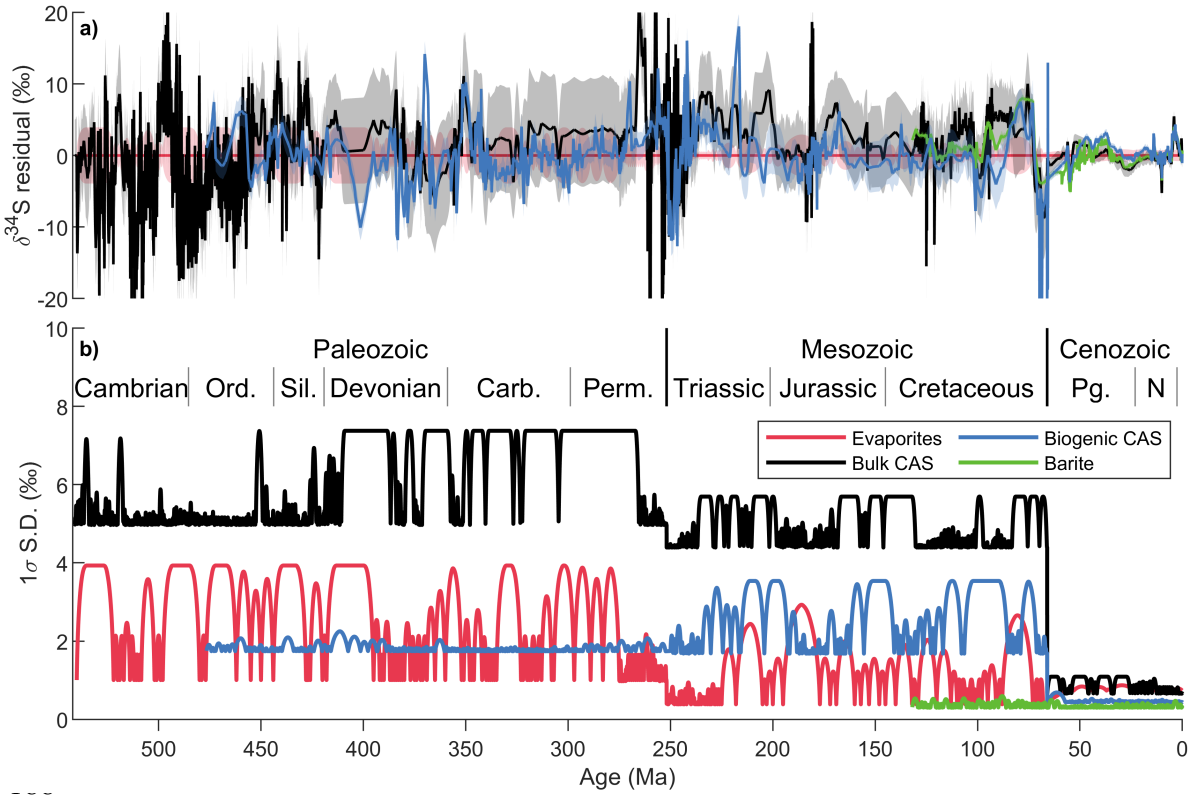

Figure 2. Comparison of δ^{34}S values and variance generated from proxy materials. **(a)** Residuals between the evaporite record and each other record shaded with kriged 1σ confidence intervals. **(b)** Confidence intervals produced from kriging data from each proxy in each era. Where data is sparse, the confidence intervals approach the standard deviation of linearly detrended data in each geologic era, excluding 1st and 99th percentile outliers. Where there is data, the confidence interval is the uncorrelated chatter determined from the semivariance of data temporally closer than the mean minimum time between data pairs.

3.2 Sources of δ^{34}S variance

The δ^{34}S variability for each proxy is plotted in Figure 2b. The maxima in each era on each curve represents the standard deviation of detrended δ^{34}S data over each geologic era. For example, the standard deviation of linearly detrended Paleozoic bulk CAS data is 7.4‰ (excluding 1st and 99th percentile outliers), while that of all Cenozoic barite data is 1.3‰. These standard deviations can be interpreted as a naive description of expected variability where data is sparse, and reflect the combination of local spatiotemporal trends in the proxy record plus an uncorrelated random component. The uncorrelated, random component is estimated by the semivariance of pairs of data that are closer together than the mean

minimum time between all pairs of data (Gebbers, 2010). The uncorrelated variances for each proxy are plotted as the minima in each era on each curve in Figure 2b.

Uncorrelated variance is a metric that convolves multiple sources of uncertainty. Sources of variance of geologic interest include temporally unresolved variability in seawater $\delta^{34}S$ values and temporally incoherent variability in how the sedimentary archives were formed or altered. These sources of variance may be temporally unresolved due either to spatial variability of seawater sulfate's $\delta^{34}S$ at a given time, or to temporal variability more rapid than the resolution of the record. In addition, the uncorrelated variance captures analytical uncertainty related to making $\delta^{34}S$ measurements in each archive, and non-systematic error in age assignments of proxy materials. While the relative contributions of each of these sources of uncertainty may differ between proxies or with age, the uncorrelated variance metric—like the population variance—describes the data's structure and how predictive a given $\delta^{34}S$ measurement is of other nearby values.

This analysis produced two key results: the uncorrelated variance is different for each archive, and for all archives it increases with age. Cenozoic and Mesozoic CAS data have uncorrelated variance larger than that of evaporites and barite. Uncorrelated Paleozoic bulk rock CAS data have a standard deviation more than twice that of biogenic CAS and evaporites. Differences between multiple proxies of the same age indicate that the uncorrelated variance is likely caused, in part, by variability inherent to how $\delta^{34}S$ is preserved, rather than just inadequate sampling of primary spatial and temporal variability of seawater sulfate.

The remaining analysis considers the sources of variance in each archive that may have contributed to the uncorrelated variance. Importantly, trends statistically distinguishable from the uncorrelated variance need not represent true trends in the $\delta^{34}S$ of Phanerozoic seawater. The same sources of variance controlling the uncorrelated data may themselves have spatial or temporal components that lead to biased estimates of Phanerozoic seawater's composition in the proxy records. The uncorrelated variance, in part, quantifies the disagreement between contemporaneous records from different localities. Trends in the data smaller than the uncorrelated variance are indistinguishable from random noise. This is true even for individual records from stratigraphic successions with coherent $\delta^{34}S$ trends: a given stratigraphic succession may clearly resolve a trend in the $\delta^{34}S$ of the proxy but fail to statistically resolve a global trend in the $\delta^{34}S$ of seawater sulfate.

3.2.1 Evaporites

Deposits of carbonate, sulfate, and halide salts form as seawater evaporates in restricted basins. Throughout Phanerozoic time, bedded marine evaporites formed subaqueously, in salinas (hypersaline lagoons) and salt pans, and subaerially, in supratidal sabkha environments. Extremely thick (>100s of meters) evaporite deposits have also formed in deeper-water environments. Deposition and preservation of evaporites require favorable climatic and tectonic conditions where restricted basins experience net evaporation (Warren,

2010). Therefore, the evaporite record has limited spatial and temporal continuity (Claypool et al., 1980; Strauss, 1997).

Because evaporites are massive products of seawater sulfate, they are largely expected to provide an accurate proxy for the $\delta^{34}S$ of ancient seawater sulfate. However, because they form in marginal marine environments often with biologically adverse salinities, it can be difficult to constrain their geologic age with biostratigraphy. In many deposits, it is also challenging to discern depositional environment or deconvolve marine and non-marine geochemical signatures (Hardie, 1984; Kendall & Harwood, 1989; Lu & Meyers, 2003). The restricted, marginal marine settings in which many evaporites form are prone to changes in fluid source or depositional environment with minor base-level changes (Playà et al., 2007). Basins rich in evaporites also often form diapirs that drive salt tectonics, which complicates a deposit's internal stratigraphy (Nielsen, 1989).

Evaporites can have a $\delta^{34}S$ range of 1‰ to 6‰ within a formation (Thode & Monster, 1965). This variability cannot be attributed to fractionation during gypsum precipitation, which produces sulfate salt prior to halite saturation that has a $\delta^{34}S$ composition 1‰ to 2‰ higher than the unevaporated seawater (Raab & Spiro, 1991). Salinity stratification in evaporating basins can promote water-column anoxia and allows MSR to distill sulfate to higher $\delta^{34}S$ compositions than the original seawater; in some cases, evaporite $\delta^{34}S$ compositions are higher than other proxies from the same depositional basin (Fike & Grotzinger, 2010). Consequently, early workers hypothesized that the isotopic composition of ancient seawater was best reflected by the lowest $\delta^{34}S$ value in an evaporite succession (Ault & Kulp, 1959; Davies & Krouse, 1975; Thode & Monster, 1965). However, evaporite basins in marginal marine environments are recharged not only by unadulterated seawater, but also by groundwater and runoff with $\delta^{34}S$ compositions biased either higher or lower than seawater from remobilized older evaporite deposits or weathered sedimentary pyrite and organic sulfur (Nielsen & Ricke, 1964; Utrilla et al., 1992). Finally, high organic carbon concentrations in many evaporite deposits can promote isotope fractionation by thermochemical sulfate reduction during burial diagenesis (Vinogradov, 2007).

Some of the uncorrelated variance in evaporite isotope ratio data also results from poor stratigraphic control (Supporting Information). Here we used updated stratigraphic information to better constrain the age of evaporite data, but the record can further benefit from higher-resolution sample collection with improved stratigraphic control during intervals where $\delta^{34}S$ changes appear in other records. Modern stratigraphic models permit correlation of evaporitic strata to better-constrained carbonate and clastic strata. Bernasconi et al. (2017) recently produced a high-resolution evaporite record that resolved the major early Triassic $\delta^{34}S$ excursions seen in earlier datasets; thus careful correlation and assignment of geologic ages permits tracking changes in the Phanerozoic sulfur cycle with evaporites. Indeed, the stratigraphic control for Mesozoic evaporites provided by Bernasconi et al. (2017) likely drives the low standard deviation of uncorrelated Mesozoic evaporite data to values (0.4‰) comparable to that of the marine barite record (0.3‰).

3.2.2 Barite

Barite precipitates from hydrothermal fluids, sediment pore fluids, and from particles within the marine water column (Paytan et al., 1993, 2002). Barite is under-saturated in most of the oceans (Chow & Goldberg, 1960; Church & Wolgemuth, 1972). However, barite has been observed in sediment traps in the upper 200 m in the water column, especially in high-productivity regions, and is associated with sulfate enrichment from decaying organic matter (Bishop, 1988). While barite super-saturation is achieved predominately by the addition of sulfate from oxidizing organic sulfur (Horner et al., 2017; Jacquet et al., 2007), marine barite apparently precipitates with $\delta^{34}S$ values within 0.4‰ of modern seawater (Paytan et al., 1998, 2002). Barite is subsequently transported to sediments by fecal pellets and marine snow (Bishop, 1988), and preserved in oxic marine sediments in high-productivity regions where enough barite is delivered to saturate pore fluids (Church & Wolgemuth, 1972). Sulfate reduction in anoxic sediments can cause dissolution of barite, which re-precipitates at the base of the sulfate reduction zone with extremely high $\delta^{34}S$ compositions (M. E. Torres et al., 1996).

Marine barite is considered an accurate proxy for ancient seawater $\delta^{34}S$ because it precipitates in the open-ocean water column and is texturally distinguishable from diagenetic barite that forms in anoxic sediments at redox fronts (Paytan et al., 1993). However, the marine barite record is limited by the availability of open-marine sediments that deposited in high-productivity regions where both authigenic enrichment of barite occurs and pore fluid sulfate concentrations remain above zero (Paytan et al., 1993). Consequently, the barite $\delta^{34}S$ record is unlikely to be extended much further than the current dataset spanning the last 130 Myr. Bedded barite deposits are associated with economically-important disulfide mineral deposits (C. A. Johnson et al., 2009), but contain large $\delta^{34}S$ variability (>10‰) and do not resolve the ancient seawater record any better than other proxy materials. Additionally, with few exceptions (e.g., Yao et al., 2018), the temporal resolution of the marine barite $\delta^{34}S$ record is unlikely to dramatically improve, especially during biogeochemical events characterized by low marine productivity (such as the Cretaceous-Paleogene boundary) or bottom-water anoxia (such as ocean anoxic events) that would have limited authigenic barite enrichment or preservation.

3.2.3 Carbonate-associated sulfate

Limestones and dolomites deposited continuously throughout Phanerozoic time, accumulating in marginal marine and open-ocean environments. A minor amount of sulfate is incorporated into biogenic and abiogenic carbonate phases. Biogenic carbonates often contain part-per-thousand sulfate by mass, while inorganic cements typically contain hundreds of parts-per-million (Barkan et al., 2020; Busenberg & Plummer, 1985; Giri & Swart, 2019; Paris, Fehrenbacher, et al., 2014; Staudt & Schoonen, 1995). Recent sediments from various peritidal carbonate platform environments include CAS with an isotopic composition similar to modern seawater (Lyons et al., 2004). CAS, therefore, complements

and exceeds the temporal resolution and completeness of the evaporite and barite records (Strauss, 1997).

Diagenetic processes may exchange sulfate with the primary carbonate and alter its isotopic composition (Fichtner et al., 2017; Murray et al., 2020; Present et al., 2015, 2019). Kampschulte & Strauss (2004) suggested that the variability of multiple $\delta^{34}S$ analyses from contemporaneous stratigraphic successions could be used to quantify the effect of diagenesis on the CAS record. However, rapidly-changing and disparate CAS $\delta^{34}S$ compositions have since been generated and interpreted—especially in Paleozoic studies—as intervals of heterogeneous seawater sulfate $\delta^{34}S$ reflecting periods of low sulfate concentrations and low marine sulfate residence times (e.g., Gill, Lyons, Young, et al., 2011; Kah et al., 2004).

Limestones and dolomites are comprised of mud or grains that precipitated both biologically and abiotically from seawater, with cements binding them together. Each of these components may recrystallize in pore fluids whose chemical composition reflects marine, meteoric, and burial diagenetic processes. A combustion CAS analysis typically requires 10 g to 100 g of carbonate (Wotte et al., 2012), and this mass requirement dictates that samples mix components that may have precipitated and/or recrystallized at different times. Further, CAS analyses may be contaminated by sulfur from co-occurring phases, including sulfide and disulfide minerals, sulfur-bearing organic material, and sulfate salts (Edwards et al., 2019; Marenco, Corsetti, Hammond, et al., 2008; Present et al., 2015; Theiling & Coleman, 2015; Wotte et al., 2012). Recent application of plasma-source mass spectrometry for sulfur isotope analysis has permitted $\delta^{34}S$ analyses on less than one-thousandth as much sulfate, corresponding to 5 mg to 50 mg of carbonate (Paris, Adkins, et al., 2014; Paris et al., 2013; Present et al., 2015, 2019; Rennie et al., 2018). Well-preserved biogenic grains, recrystallized grains, matrix, and cements contain CAS with $\delta^{34}S$ compositions varying by as much as 25‰, spanning most of range of CAS analyses from the entire Phanerozoic (Present et al., 2015, 2019). Therefore, much of the variability of CAS $\delta^{34}S$ data may not reflect the $\delta^{34}S$ composition of ancient seawater sulfate. Identifying components that retain the $\delta^{34}S$ of sulfate incorporated from syndepositional seawater is critical to precisely and accurately exploit the CAS $\delta^{34}S$ archive.

CAS can reflect the $\delta^{34}S$ of syndepositional seawater sulfate if the carbonate component did not recrystallize after precipitation, if recrystallization and cementation occurred in contact with a low-sulfate fluid, or if the $\delta^{34}S$ of pore fluid sulfate was not fractionated from seawater (Gill et al., 2008; Lyons et al., 2004; Rennie & Turchyn, 2014). Alteration occurs if the sediments recrystallize above the depth at which sulfate is completely consumed by MSR but deep enough that some distillation of $\delta^{34}S$ within sediment pore fluid has occurred (Edwards et al., 2019; Fike et al., 2015; Present et al., 2019; Rennie & Turchyn, 2014; Witts et al., 2018). Additionally, some ancient carbonates contain CAS with anomalously low $\delta^{34}S$ interpreted to result from the incorporation of sulfate from sulfide that was reoxidized during diagenesis or weathering (Baldermann et al., 2015; Edwards et al., 2019; Fichtner et al., 2017; Fike et al., 2015; Marenco, Corsetti, Kaufman, et al., 2008; Present et al., 2015, 2019; Rennie & Turchyn, 2014; Riccardi et al., 2006; Yan et al., 2013). Carbonates recrystallizing

during burial may also be prone to diagenetic modification of the $\delta^{34}S$ of CAS if the burial fluids were sulfate rich (Fichtner et al., 2017, 2018; Present et al., 2015). The $\delta^{34}S$ in burial fluids may be highly variable, and include sulfate from hydrocarbon or organic matter degradation, dissolved evaporites, groundwater modified by MSR, or sulfate released by dissolution of CAS (Dogramaci et al., 2001; Fichtner et al., 2018; Murray et al., 2020; Present et al., 2019; Thode & Monster, 1965, 1970).

These diagenetic controls on the $\delta^{34}S$ of CAS decrease the precision and accuracy of the proxy. This is quantified by its uncorrelated variance, which is much higher than that observed in other seawater sulfate $\delta^{34}S$ proxies. Uncorrelated Paleozoic CAS data has a standard deviation of 5.0‰, and that of Mesozoic CAS is 4.4‰, which is five to ten times larger than that of Paleozoic and Mesozoic evaporites (1.0‰ and 0.4‰, respectively). Further, diagenesis may have impacted accuracy by systematically biasing the $\delta^{34}S$ of CAS with respect to the primary composition of seawater sulfate. For example, base level often controls the stratigraphic arrangement of facies in carbonates successions, which can impart biases as large as 10‰ on the $\delta^{34}S$ of CAS (Present et al., 2019; Richardson, Keating, et al., 2019). Both the random and systematic variability is on the order of well-resolved rapid changes of 3‰ to 6‰ in the $\delta^{34}S$ of marine barite and biogenic CAS.

3.2.4 Biogenic CAS

Biogenic CAS may offer a more robust $\delta^{34}S$ record than bulk CAS because biogenic carbonate can often be readily separated from other limestone components, preservation quality can be assessed, and vital effects appear to be small in most taxa (Kampschulte et al., 2001; Paris, Fehrenbacher, et al., 2014; Present et al., 2015). In modern and cultured biogenic carbonates, the incorporated sulfate has an isotopic composition within 2‰ of the seawater from which it precipitated (Burdett et al., 1989; Kampschulte et al., 2001; Kaplan et al., 1963; Mekhtiyeva, 1974; Paris et al., 2013; Paris, Fehrenbacher, et al., 2014; Present et al., 2015). Recently, Rennie et al. (2018) produced a taxon-specific foraminiferal CAS record with variance and secular trends comparable to the marine barite record.

Low-magnesium calcite, precipitated by many brachiopods, belemnites, and planktonic foraminifera, is stable at Earth's surface and shallow burial conditions. The low-magnesium calcite biogenic CAS $\delta^{34}S$ record has significantly improved the resolution of the Phanerozoic $\delta^{34}S$ record during two key periods. First, during the Toarcian (Jurassic) Ocean Anoxic Event, belemnite CAS displays a large (6‰) $\delta^{34}S$ excursion that is not well resolved in the evaporite record (Gill, Lyons, & Jenkyns, 2011; Newton et al., 2011). Second, during Carboniferous time, brachiopods record a prolonged recovery from a $\delta^{34}S$ maximum in middle Devonian time (D. L. Johnson et al., 2020; Kampschulte et al., 2001; N. Wu et al., 2014). However, aragonite and high-magnesium calcite, precipitated by many bivalves, gastropods, corals, trilobites, echinoderms, bryozoans, and marine algae, dissolves and/or recrystallizes much more readily than low-magnesium calcite (Brand & Veizer, 1980). Few studies have investigated CAS $\delta^{34}S$ from formerly aragonitic fossils (Mekhtiyeva, 1974; Present et al., 2015; Witts et al., 2018).

Unfortunately, well-preserved biogenic carbonate is rare in the rock record, especially during intervals of climatic or biologic crisis (e.g., mass extinction events). Even apparently well-preserved biogenic carbonate can still be susceptible to diagenetic alteration (Fichtner et al., 2018; Witts et al., 2018). Like the marine barite record, a significant expansion of the biogenic CAS $\delta^{34}S$ proxy record is limited by the availability of suitable sample material.

3.3 Discrepant early Phanerozoic proxy records

While all archives imperfectly estimate ancient seawater's composition, they provide generally indistinguishable estimates considering the sources of uncertainty discussed (Figure 2a). Paleozoic bulk rock CAS data, as a notable exception, commonly exhibit rapid $\delta^{34}S$ variability (Figure 1b), but other archives with less uncorrelated variance are absent or lack temporal resolution (Figure 1a). Throughout Phanerozoic strata, CAS data consistently display more unresolved variance than other archives, yet they record the same long-term trends (Figure 2), suggesting that some $\delta^{34}S$ excursions recorded by CAS may not represent changes in the composition of the ocean. The high uncorrelated variance in all early Paleozoic archives may mask $\delta^{34}S$ excursions on the order of those well-resolved in younger strata by all archives. Spatial and temporal variability in early Paleozoic CAS data may represent short residence times of sulfate in sulfidic oceans (e.g., Gill, Lyons, Young, et al., 2011; Kah et al., 2016), local diagenetic effects on the $\delta^{34}S$ of carbonate rocks (Present et al., 2015, 2019; Richardson, Keating, et al., 2019; Richardson, Newville, et al., 2019), or both (Edwards et al., 2019; Rose et al., 2019).

CAS $\delta^{34}S$ excursions often correlate with global perturbations evidenced by carbon isotope excursions and trace metal, pyrite sulfur isotope, and bioturbation intensity records (Canfield & Farquhar, 2009; Fike et al., 2015; Gill et al., 2007; Jones & Fike, 2013; Kah et al., 2016; Saltzman et al., 2015). Perhaps some CAS $\delta^{34}S$ excursions reflect widespread biogeochemical changes at the interface between pore fluid sulfur cycling and carbonate sediment diagenesis, including sulfate, dioxygen, and nutrient availability, organic productivity, or metabolic or oceanographic changes in carbonate mineral saturation (Rennie & Turchyn, 2014). Because part of the $\delta^{34}S$ variance in all archives derives from early diagenetic processes—such as MSR, pyrite formation, and sulfide reoxidation—consideration of these processes may reveal important temporal changes in carbon cycling in marine pore fluids (Present et al., 2019; Richardson, Keating, et al., 2019; N. Wu et al., 2010).

4 Conclusions

Phanerozoic $\delta^{34}S$ data were compiled from evaporites, barite, biogenic CAS, and bulk rock CAS and updated to a consistent time scale. The subset of seawater sulfate's $\delta^{34}S$ history possibly sampled by each proxy varied in space and time, and different suites of depositional and post-depositional processes added variance to each archive. The variance in each record increases with age, but the changing contribution of primary and secondary sources of variability over Phanerozoic time remains unclear.

Bulk CAS contains a statistically significant different distribution of $\delta^{34}S$ compositions than the biogenic CAS, evaporite, or barite records. Early diagenetic overprinting of CAS occurs in depositional environments where carbonate recrystallization and cementation coincides with sulfate-rich pore fluids with modified $\delta^{34}S$ values. Despite these complications, bulk CAS can be widely applied in ancient sedimentary basins and is the only archive readily able to resolve sulfur cycle changes during rapid biogeochemical events. Extending the breadth and resolution of the $\delta^{34}S$ record requires developing mechanistic understanding of how biogeochemical perturbations affect the marine diagenesis of carbonate rocks.

Acknowledgements

No new data were collected for this study. Datasets compiled for this research are tabulated in the Supplemental Material and referenced below. We thank Caltech DocuServe for obtaining many of the publications containing the compiled data, and John Grotzinger and Joe Kirschvink for thoughtful advising and feedback. Constructive reviews by Akshay Mehra and Julia Wilcots were greatly appreciated.

References

Adams, D. D., Hurtgen, M. T., & Sageman, B. B. (2010). Volcanic triggering of a biogeochemical cascade during Oceanic Anoxic Event 2. *Nature Geoscience*, *3*(3), 201–204. https://doi.org/10.1038/Ngeo743

Algeo, T. J., Henderson, C. M., Tong, J., Feng, Q., Yin, H., & Tyson, R. V. (2013). Plankton and productivity during the Permian–Triassic boundary crisis: An analysis of organic carbon fluxes. *Global and Planetary Change*, *105*, 52–67. https://doi.org/10.1016/j.gloplacha.2012.02.008

Arp, G., Ostertag-Henning, C., YÜCekent, S., Reitner, J., & Thiel, V. (2008). Methane-related microbial gypsum calcitization in stromatolites of a marine evaporative setting (Münder Formation, Upper Jurassic, Hils Syncline, north Germany). *Sedimentology*, *55*(5), 1227–1251. https://doi.org/10.1111/j.1365-3091.2007.00944.x

Ault, W. U., & Kulp, J. L. (1959). Isotopic geochemistry of sulphur. *Geochimica et Cosmochimica Acta*, *16*(4), 201–235. https://doi.org/10.1016/0016-7037(59)90112-7

Balderer, W., Pearson, F. J., & Soreau, S. (1991). Formation-Specific Characterization of Groundwaters. In F. J. Pearson, W. Balderer, H. H. Loosli, B. E. Lehmann, A. Matter, T. Peters, et al. (Eds.), *Applied Isotope Hydrogeology: A Case Study in Northern Switzerland: Technical Report 88-01* (pp. 297–374). Amsterdam: Elsevier. Retrieved from https://books.google.com/books?id=fEBs7PudzAEC

Baldermann, A., Deditius, A. P., Dietzel, M., Fichtner, V., Fischer, C., Hippler, D., et al. (2015). The role of bacterial sulfate reduction during dolomite precipitation: Implications from Upper Jurassic platform carbonates. *Chemical Geology*, *412*, 1–14. https://doi.org/10.1016/j.chemgeo.2015.07.020

Barkan, Y., Paris, G., Webb, S. M., Adkins, J. F., & Halevy, I. (2020). Sulfur isotope fractionation between aqueous and carbonate-associated sulfate in abiotic calcite and aragonite. *Geochimica et Cosmochimica Acta*. https://doi.org/10.1016/j.gca.2020.03.022

Ben-Yaakov, S. (1973). pH Buffering of Pore Water of Recent Anoxic Marine Sediments. *Limnology and Oceanography*, *18*(1), 86–94. https://doi.org/10.4319/lo.1973.18.1.0086

Berggren, W. A., Kent, D. V., Flynn, J. J., & Van Couvering, J. A. (1985). Cenozoic geochronology. *Geological Society of America Bulletin*, *96*, 1407–1418.

Berggren, W. A., Kent, D. V., Swisher, C. C., & Aubry, M.-P. (1995). A Revised Cenozoic Geochronology and Chronostratigraphy. In *Geochronology, Time Scales and Global Stratigraphic Correlation* (pp. 129–212). SEPM (Society for Sedimentary Geology). https://doi.org/10.2110/pec.95.04.0129

Bergström, S. M., Chen, X., Gutiérrez-Marco, J. C., & Dronov, A. (2009). The new chronostratigraphic classification of the Ordovician System and its relations to major regional series and stages and to δ13C chemostratigraphy. *Lethaia*, *42*(1), 97–107. https://doi.org/10.1111/j.1502-3931.2008.00136.x

Bernasconi, S. M., Meier, I., Wohlwend, S., Brack, P., Hochuli, P. A., Bläsi, H., et al. (2017). An evaporite-based high-resolution sulfur isotope record of Late Permian and Triassic seawater sulfate. *Geochimica et Cosmochimica Acta*, *204*, 331–349. https://doi.org/10.1016/j.gca.2017.01.047

Bishop, J. K. B. (1988). The barite-opal-organic carbon association in oceanic particulate matter. *Nature*, *332*(6162), 341–343. https://doi.org/10.1038/332341a0

Blomquist, P. K. (2016). Wolfcamp Horizontal Play, Midland Basin, West Texas, #10890 (2016). In *AAPG Pacific Section and Rocky Mountain Section Joint Meeting* (p. 34). Las Vegas, Nevada. Retrieved from http://www.searchanddiscovery.com/pdfz/documents/2016/10890blomquist/ndx_blomquist.pdf.html

Boschetti, T., Cortecchi, G., Toscani, L., & Iacumin, P. (2011). Sulfur and oxygen isotope compositions of Upper Triassic sulfates from Northerm Apennines (Italy): palaeogeographic and hidrogeochemical implications. *Geologica Acta*, *9*(2), 129–147. https://doi.org/10.1344/105.000001690

Bottrell, S. H., & Newton, R. J. (2006). Reconstruction of changes in global sulfur cycling from marine sulfate isotopes. *Earth-Science Reviews*, *75*(1–4), 59–83. https://doi.org/10.1016/j.earscirev.2005.10.004

Bowles, M. W., Mogollón, J. M., Kasten, S., Zabel, M., & Hinrichs, K.-U. (2014). Global rates of marine sulfate reduction and implications for sub–sea-floor metabolic activities. *Science*, *344*(6186), 889. https://doi.org/10.1126/science.1249213

Bowring, S. A., Erwin, D. H., Jin, Y. G., Martin, M. W., Davidek, K., & Wang, W. (1998). U/Pb Zircon Geochronology and Tempo of the End-Permian Mass Extinction. *Science*, *280*(5366), 1039–1045. https://doi.org/10.1126/science.280.5366.1039

Bradley, A. S., Leavitt, W. D., Schmidt, M., Knoll, A. H., Girguis, P. R., & Johnston, D. T. (2016). Patterns of sulfur isotope fractionation during microbial sulfate reduction. *Geobiology*, *14*(1), 91–101. https://doi.org/10.1111/gbi.12149

Brand, U., & Veizer, J. (1980). Chemical diagenesis of a multicomponent carbonate system; 1, Trace elements. *Journal of Sedimentary Research*, *50*(4), 1219–1236. https://doi.org/10.1306/212f7bb7-2b24-11d7-8648000102c1865d

Burdett, J. W., Arthur, M. A., & Richardson, M. (1989). A Neogene seawater sulfur isotope age curve from calcareous pelagic microfossils. *Earth and Planetary Science Letters*, *94*, 189–198. https://doi.org/10.1016/0012-821x(89)90138-6

Burgess, S. D., Bowring, S., & Shen, S. (2014). High-precision timeline for Earth's most severe extinction. *Proceedings of the National Academy of Sciences*. https://doi.org/10.1073/pnas.1317692111

Burke, A., Present, T. M., Paris, G., Rae, E. C. M., Sandilands, B. H., Gaillardet, J., et al. (2018). Sulfur isotopes in rivers: Insights into global weathering budgets, pyrite oxidation, and the modern sulfur cycle. *Earth and Planetary Science Letters*. https://doi.org/10.1016/j.epsl.2018.05.022

Buschendorf, Fr., Nielsen, H., Puchelt, H., & Ricke, W. (1963). Schwefel-Isotopen-Untersuchungen am Pyrit-Sphalerit-Baryt-Lager Meggen/Lenne (Deutschland) und an verschiedenen Devon-Evaporiten. *Geochimica et Cosmochimica Acta*, *27*(5), 501–523. https://doi.org/10.1016/0016-7037(63)90085-1

Busenberg, E., & Plummer, N. L. (1985). Kinetic and thermodynamic factors controlling the distribution of SO42− and Na+ in calcites and selected aragonites. *Geochimica et Cosmochimica Acta*, *49*(3), 713–725. https://doi.org/10.1016/0016-7037(85)90166-8

Cai, C., Hu, W., & Worden, R. H. (2001). Thermochemical sulphate reduction in Cambro–Ordovician carbonates in Central Tarim. *Marine and Petroleum Geology*, *18*(6), 729–741. https://doi.org/10.1016/S0264-8172(01)00028-9

Canfield, D. E., & Farquhar, J. (2009). Animal evolution, bioturbation, and the sulfate concentration of the oceans. *Proceedings of the National Academy of Sciences*, *106*(20), 8123–8127. https://doi.org/10.1073/pnas.0902037106

Chen, D., Wang, J., Racki, G., Li, H., Wang, C., Ma, X., & Whalen, M. T. (2013). Large sulphur isotopic perturbations and oceanic changes during the Frasnian–Famennian transition of the Late Devonian. *Journal of the Geological Society*, *170*(3), 465–476. https://doi.org/10.1144/jgs2012-037

Chen, J., Zhao, R., Huo, W., Yao Yuyuan Pan, S., Shao, M., & Hai, C. (1981). Sulfur Isotopes of Some Marine Gypsum. *Chinese Journal of Geology*, *3*, 009.

Chow, T. J., & Goldberg, E. D. (1960). On the marine geochemistry of barium. *Geochimica et Cosmochimica Acta*, *20*(3), 192–198. https://doi.org/10.1016/0016-7037(60)90073-9

Church, T. M., & Wolgemuth, K. (1972). Marine barite saturation. *Earth and Planetary Science Letters*, *15*(1), 35–44. https://doi.org/10.1016/0012-821X(72)90026-X

Claypool, G. E., Holser, W. T., Kaplan, I. R., Sakai, H., & Zak, I. (1980). The age curves of sulfur and oxygen isotopes in marine sulfate and their mutual interpretation. *Chemical Geology*, *28*, 199–260. https://doi.org/10.1016/0009-2541(80)90047-9

Cohen, K., Finney, S., Gibbard, P., & Fan, J.-X. (2013). The ICS international chronostratigraphic chart. *Episodes*, *36*(3), 199–204.

Cortecci, G., Reyes, E., Berti, G., & Casati, P. (1981). Sulfur and oxygen isotopes in Italian marine sulfates of Permian and Triassic ages. *Chemical Geology*, *34*(1), 65–79. https://doi.org/10.1016/0009-2541(81)90072-3

Cramer, B. D., Loydell, D. K., Samtleben, C., Munnecke, A., Kaljo, D., Männik, P., et al. (2010). Testing the limits of Paleozoic chronostratigraphic correlation via high-resolution (<500 k.y.) integrated conodont, graptolite, and carbon isotope (δ13Ccarb)

biochemostratigraphy across the Llandovery–Wenlock (Silurian) boundary: Is a unified Phanerozoic time scale achievable? *Geological Society of America Bulletin*, 17.

Cramer, B. D., Condon, D. J., Söderlund, U., Marshall, C., Worton, G. J., Thomas, A. T., et al. (2012). U-Pb (zircon) age constraints on the timing and duration of Wenlock (Silurian) paleocommunity collapse and recovery during the "Big Crisis." *GSA Bulletin*, *124*(11–12), 1841–1857. https://doi.org/10.1130/B30642.1

Cressie, N., & Hawkins, D. M. (1980). Robust estimation of the variogram: I. *Journal of the International Association for Mathematical Geology*, *12*(2), 115–125. https://doi.org/10.1007/BF01035243

Dahl, T. W., Connelly, J. N., Li, D., Kouchinsky, A., Gill, B. C., Porter, S., et al. (2019). Atmosphere–ocean oxygen and productivity dynamics during early animal radiations. *Proceedings of the National Academy of Sciences*, *116*(39), 19352–19361. https://doi.org/10.1073/pnas.1901178116

Das, N., Horita, J., & Holland, H. D. (1990). Chemistry of fluid inclusions in halite from the Salina Group of the Michigan basin: Implications for Late Silurian seawater and the origin of sedimentary brines. *Geochimica et Cosmochimica Acta*, *54*(2), 319–327. https://doi.org/10.1016/0016-7037(90)90321-B

Davies, G. R., & Krouse, H. R. (1975). Sulphur isotope distribution in Paleozoic sulphate evaporites, Canadian Arctic Archipelago. *Geological Survey of Canada Paper*, *75–1 Part B*, 221–225.

Dogramaci, S. S., Herczeg, A. L., Schiff, S. L., & Bone, Y. (2001). Controls on δ34S and δ18O of dissolved sulfate in aquifers of the Murray Basin, Australia and their use as indicators of flow processes. *Applied Geochemistry*, *16*(4), 475–488. https://doi.org/10.1016/S0883-2927(00)00052-4

Edwards, C. T., Fike, D. A., Saltzman, M. R., Lu, W., & Lu, Z. (2018). Evidence for local and global redox conditions at an Early Ordovician (Tremadocian) mass extinction. *Earth and Planetary Science Letters*, *481*, 125–135. https://doi.org/10.1016/j.epsl.2017.10.002

Edwards, C. T., Fike, D. A., & Saltzman, M. R. (2019). Testing carbonate-associated sulfate (CAS) extraction methods for sulfur isotope stratigraphy: A case study of a Lower–Middle Ordovician carbonate succession, Shingle Pass, Nevada, USA. *Chemical Geology*, *529*, 119297. https://doi.org/10.1016/j.chemgeo.2019.119297

van Everdingen, R. O., Shakur, M. A., & Krouse, H. R. (1982). 34S and 18O abundances differentiate Upper Cambrian and Lower Devonian gypsum-bearing units, District of Mackenzie, N.W.T.—an update. *Canadian Journal of Earth Sciences*, *19*(6), 1246–1254. https://doi.org/10.1139/e82-106

Fanlo, I., & Ayora, C. (1998). The evolution of the Lorraine evaporite basin: implications for the chemical and isotope composition of the Triassic ocean. *Chemical Geology*, *146*(3), 135–154. https://doi.org/10.1016/S0009-2541(98)00007-2

Feely, H. W., & Kulp, J. L. (1957). Origin of Gulf Coast Salt-Dome Sulphur Deposits. *AAPG Bulletin*, *41*(8), 1802–1853.

Fichtner, V., Strauss, H., Immenhauser, A., Buhl, D., Neuser, R. D., & Niedermayr, A. (2017). Diagenesis of carbonate associated sulfate. *Chemical Geology*, *463*(Supplement C), 61–75. https://doi.org/10.1016/j.chemgeo.2017.05.008

Fichtner, V., Strauss, H., Mavromatis, V., Dietzel, M., Huthwelker, T., Borca, C. N., et al. (2018). Incorporation and subsequent diagenetic alteration of sulfur in Arctica islandica. *Chemical Geology*, *482*, 72–90. https://doi.org/10.1016/j.chemgeo.2018.01.035

Fike, D. A., & Grotzinger, J. P. (2008). A paired sulfate–pyrite δ34S approach to understanding the evolution of the Ediacaran–Cambrian sulfur cycle. *Geochimica et Cosmochimica Acta*, *72*(11), 2636–2648. https://doi.org/10.1016/j.gca.2008.03.021

Fike, D. A., & Grotzinger, J. P. (2010). A δ34SSO4 approach to reconstructing biogenic pyrite burial in carbonate-evaporite basins: An example from the Ara Group, Sultanate of Oman. *Geology*, *38*, 371–374.

Fike, D. A., Bradley, A. S., & Rose, C. V. (2015). Rethinking the Ancient Sulfur Cycle. *Annual Review of Earth and Planetary Sciences*, *43*(1), 593–622. https://doi.org/10.1146/annurev-earth-060313-054802

Fox, J. S., & Videtich, P. E. (1997). Revised estimate of δ34S for marine sulfates from the Upper Ordovician: data from the Williston Basin, North Dakota, U.S.A. *Applied Geochemistry*, *12*(1), 97–103. https://doi.org/10.1016/S0883-2927(96)00065-0

Froelich, P. N., Klinkhammer, G. P., Bender, M. L., Luedtke, N. A., Heath, G. R., Cullen, D., et al. (1979). Early oxidation of organic matter in pelagic sediments of the eastern equatorial Atlantic: suboxic diagenesis. *Geochimica et Cosmochimica Acta*, *43*, 1075–1090. https://doi.org/10.1016/0016-7037(79)90095-4

Gebbers, R. (2010). Geostatistics and Kriging. In M. H. Trauth, *MATLAB Recipes for Earth Sciences* (3rd Ed., pp. 235–254). Berlin, Germany: Springer-Verlag.

Gill, B. C., Lyons, T. W., & Saltzman, M. R. (2007). Parallel, high-resolution carbon and sulfur isotope records of the evolving Paleozoic marine sulfur reservoir. *Palaeogeography, Palaeoclimatology, Palaeoecology*, *256*, 156–173. https://doi.org/10.1016/j.palaeo.2007.02.030

Gill, B. C., Lyons, T. W., & Frank, T. D. (2008). Behavior of carbonate-associated sulfate during meteoric diagenesis and implications for the sulfur isotope paleoproxy. *Geochimica et Cosmochimica Acta*, *72*, 4699–4711. https://doi.org/10.1016/j.gca.2008.07.001

Gill, B. C., Lyons, T. W., & Jenkyns, H. C. (2011). A global perturbation to the sulfur cycle during the Toarcian Oceanic Anoxic Event. *Earth and Planetary Science Letters*, *312*, 484–496. https://doi.org/10.1016/j.epsl.2011.10.030

Gill, B. C., Lyons, T. W., Young, S. A., Kump, L. R., Knoll, A. H., & Saltzman, M. R. (2011). Geochemical evidence for widespread euxinia in the Later Cambrian ocean. *Nature*, *469*, 80–83.

Giri, S. J., & Swart, P. K. (2019). The influence of seawater chemistry on carbonate-associated sulfate derived from coral skeletons. *Palaeogeography, Palaeoclimatology, Palaeoecology*, *521*, 72–81. https://doi.org/10.1016/j.palaeo.2019.02.011

Gomes, M. L., Hurtgen, M. T., & Sageman, B. B. (2016). Biogeochemical sulfur cycling during Cretaceous oceanic anoxic events: A comparison of OAE1a and OAE2. *Paleoceanography*, *31*(2), 2015PA002869. https://doi.org/10.1002/2015PA002869

Gorjan, P., & Kaiho, K. (2007). Correlation and comparison of seawater δ34Ssulfate records at the Permian-Triassic transition. *Chemical Geology*, *243*, 275–285. https://doi.org/10.1016/j.chemgeo.2007.03.011

Grotzinger, J. P., & Kasting, J. F. (1993). New constraints on Precambrian ocean composition. *The Journal of Geology*, 235–243.

Guo, C., Chen, D., Song, Y., Zhou, X., Ding, Y., & Zhang, G. (2018). Depositional environments and cyclicity of the Early Ordovician carbonate ramp in the western Tarim Basin (NW China). *Journal of Asian Earth Sciences*, *158*, 29–48. https://doi.org/10.1016/j.jseaes.2018.02.006

Handford, C. R., & Dutton, S. P. (1980). Pennsylvanian–Early Permian Depositional Systems and Shelf-Margin Evolution, Palo Duro Basin, Texas. *AAPG Bulletin*, *64*(1), 88–106. https://doi.org/10.1306/2F918932-16CE-11D7-8645000102C1865D

Hannisdal, B., & Peters, S. E. (2011). Phanerozoic Earth System Evolution and Marine Biodiversity. *Science*, *334*(6059), 1121–1124. https://doi.org/10.1126/science.1210695

Hardie, L. A. (1984). Evaporites; marine or non-marine? *American Journal of Science*, *284*(3), 193–240. https://doi.org/10.2475/ajs.284.3.193

Harland, W., Armstrong, R., Cox, A., Craig, L., Smith, A., & Smith, D. (1990). *A Geologic Time Scale 1989*. Cambridge University Press.

Harrison, A. G., & Thode, H. G. (1958). Mechanism of the bacterial reduction of sulphate from isotope fractionation studies. *Transactions of the Faraday Society*, *54*, 84. https://doi.org/10.1039/tf9585400084

He, T., Zhu, M., Mills, B. J. W., Wynn, P. M., Zhuravlev, A. Y., Tostevin, R., et al. (2019). Possible links between extreme oxygen perturbations and the Cambrian radiation of animals. *Nature Geoscience*, 1. https://doi.org/10.1038/s41561-019-0357-z

Hearn, M. R., Machel, H. G., & Rostron, B. J. (2011). Hydrocarbon breaching of a regional aquitard: The Devonian Ireton Formation, Bashaw area, Alberta, Canada. *AAPG Bulletin*, *95*(6), 1009–1037. https://doi.org/10.1306/09271010050

Hitchon, B., & Krouse, H. R. (1972). Hydrogeochemistry of the surface waters of the Mackenzie River drainage basin, Canada—III. Stable isotopes of oxygen, carbon and sulphur. *Geochimica et Cosmochimica Acta*, *36*(12), 1337–1357. https://doi.org/10.1016/0016-7037(72)90066-X

Holland, H. D. (1973). Systematics of the isotopic composition of sulfur in the oceans during the Phanerozoic and its implications for atmospheric oxygen. *Geochimica et Cosmochimica Acta*, *37*(12), 2605–2616. https://doi.org/10.1016/0016-7037(73)90268-8

Holser, W. T. (1977). Catastrophic chemical events in the history of the ocean. *Nature*, *267*, 403–408.

Holser, W. T., & Kaplan, I. R. (1966). Isotope geochemistry of sedimentary sulfates. *Chemical Geology*, *1*, 93–135. https://doi.org/10.1016/0009-2541(66)90011-8

Holser, W. T., Maynard, J. B., & Cruikshank, K. (1989). Modelling the natural cycle of sulphur through Phanerozoic time. *Evolution of the Global Biogeochemical Sulphur Cycle. Wiley, New York*, 21–56.

Horacek, M., Brandner, R., Richoz, S., & Povoden-Karadeniz, E. (2010). Lower Triassic sulphur isotope curve of marine sulphates from the Dolomites, N-Italy. *Palaeogeography, Palaeoclimatology, Palaeoecology*, *290*(1), 65–70. https://doi.org/10.1016/j.palaeo.2010.02.016

Horner, T. J., Pryer, H. V., Nielsen, S. G., Crockford, P. W., Gauglitz, J. M., Wing, B. A., & Ricketts, R. D. (2017). Pelagic barite precipitation at micromolar ambient sulfate. *Nature Communications*, *8*(1), 1342. https://doi.org/10.1038/s41467-017-01229-5

Hovorka, S. D., Knauth, L. P., Fisher, R. S., & Gao, G. (1993). Marine to nonmarine facies transition in Permian evaporites of the Palo Duro Basin, Texas: Geochemical response. *GSA Bulletin*, *105*(8), 1119–1134. https://doi.org/10.1130/0016-7606(1993)105<1119:MTNFTI>2.3.CO;2

Hurtgen, M. T., Pruss, S. B., & Knoll, A. H. (2009). Evaluating the relationship between the carbon and sulfur cycles in the later Cambrian ocean: An example from the Port au Port Group, western Newfoundland, Canada. *Earth and Planetary Science Letters*, *281*(3–4), 288–297. https://doi.org/10.1016/j.epsl.2009.02.033

Insalaco, E., Virgone, A., Courme, B., Gaillot, J., Kamali, M., Moallemi, A., et al. (2006). Upper Dalan Member and Kangan Formation between the Zagros Mountains and offshore Fars, Iran: depositional system, biostratigraphy and stratigraphic architecture. *GeoArabia*, *11*(2), 75–176.

Jacquet, S. H. M., Henjes, J., Dehairs, F., Worobiec, A., Savoye, N., & Cardinal, D. (2007). Particulate Ba-barite and acantharians in the Southern Ocean during the European Iron Fertilization Experiment (EIFEX). *Journal of Geophysical Research: Biogeosciences*, *112*(G4). https://doi.org/10.1029/2006JG000394

John, E. H., Wignall, P. B., Newton, R. J., & Bottrell, S. H. (2010). δ34SCAS and δ18OCAS records during the Frasnian–Famennian (Late Devonian) transition and their bearing on mass extinction models. *Chemical Geology*, *275*(3–4), 221–234. https://doi.org/10.1016/j.chemgeo.2010.05.012

Johnson, C. A., Emsbo, P., Poole, F. G., & Rye, R. O. (2009). Sulfur- and oxygen-isotopes in sediment-hosted stratiform barite deposits. *Geochimica et Cosmochimica Acta*, *73*(1), 133–147. https://doi.org/10.1016/j.gca.2008.10.011

Johnson, D. L., Grossman, E. L., Webb, S. M., & Adkins, J. F. (2020). Brachiopod δ34SCAS microanalyses indicate a dynamic, climate-influenced Permo-Carboniferous sulfur cycle. *Earth and Planetary Science Letters*, *546*, 116428. https://doi.org/10.1016/j.epsl.2020.116428

Jones, D. S., & Fike, D. A. (2013). Dynamic sulfur and carbon cycling through the end-Ordovician extinction revealed by paired sulfate–pyrite δ34S. *Earth and Planetary Science Letters*, *363*, 144–155.

Jørgensen, B. B. (1982). Mineralization of organic matter in the sea bed- the role of sulphate reduction. *Nature*, *296*, 643–645.

Kah, L. C., Lyons, T. W., & Frank, T. D. (2004). Low marine sulphate and protracted oxygenation of the Proterozoic biosphere. *Nature*, *431*, 834–838.

Kah, L. C., Thompson, C. K., Henderson, M. A., & Zhan, R. (2016). Behavior of marine sulfur in the Ordovician. *Palaeogeography, Palaeoclimatology, Palaeoecology*, *458*, 133–153. https://doi.org/10.1016/j.palaeo.2015.12.028

Kaiho, K., Kajiwara, Y., Nakano, T., Miura, Y., Kawahata, H., Tazaki, K., et al. (2001). End-Permian catastrophe by a bolide impact: Evidence of a gigantic release of sulfur from the mantle. *Geology*, *29*, 815–818. https://doi.org/10.1130/0091-7613(2001)029<0815:epcbab>2.0.co;2

Kaiho, Kunio, Kajiwara, Y., Tazaki, K., Ueshima, M., Takeda, N., Kawahata, H., et al. (1999). Oceanic primary productivity and dissolved oxygen levels at the Cretaceous/Tertiary boundary: their decrease, subsequent warming, and recovery. *Paleoceanography*, *14*(4), 511–524.

Kaiho, Kunio, Kajiwara, Y., Chen, Z.-Q., & Gorjan, P. (2006). A sulfur isotope event at the end of the Permian. *Chemical Geology*, *235*(1–2), 33–47. https://doi.org/10.1016/j.chemgeo.2006.06.001

Kampschulte, A., & Strauss, H. (2004). The sulfur isotopic evolution of Phanerozoic seawater based on the analysis of structurally substituted sulfate in carbonates. *Chemical Geology*, *204*, 255–286. https://doi.org/10.1016/j.chemgeo.2003.11.013

Kampschulte, A., Bruckschen, P., & Strauss, H. (2001). The sulphur isotopic composition of trace sulphates in Carboniferous brachiopods: implications for coeval seawater, correlation with other geochemical cycles and isotope stratigraphy. *Chemical Geology*, *175*, 149–173. https://doi.org/10.1016/s0009-2541(00)00367-3

Kampschulte, Anke. (2001). *Schwefelisotopenuntersuchungen an strukturell substituierten Sulfaten in marinen Karbonaten des Phanerozoikums : Implikationen für die geochemische Evolution des Meerwassers und die Korrelation verschiedener Stoffkreisläufe*. Ruhr-Universität Bochum. Retrieved from http://www-brs.ub.ruhr-uni-bochum.de/netahtml/HSS/Diss/KampschulteAnke/

Kaplan, I. R., Emery, K. O., & Rittenberg, S. C. (1963). The distribution and isotopic abundance of sulphur in recent marine sediments off southern California. *Geochimica et Cosmochimica Acta*, *27*(4), 297–331. https://doi.org/10.1016/0016-7037(63)90074-7

Kaufmann, B. (2006). Calibrating the Devonian Time Scale: A synthesis of U–Pb ID–TIMS ages and conodont stratigraphy. *Earth-Science Reviews*, *76*(3–4), 175–190. https://doi.org/10.1016/j.earscirev.2006.01.001

Kendall, A. C., & Harwood, G. M. (1989). Shallow-Water Gypsum in the Castile Formation - Significance and Implications. In P. M. Harris & G. A. Grover (Eds.), *Subsurface and Outcrop Examination of the Capitan Shelf Margin, Northern Delaware Basin* (pp. 451–457). San Antonio, Texas: SEPM. Retrieved from https://pubs.geoscienceworld.org/books/book/1170/chapter/10575312/shallow-water-gypsum-in-the-castile-formation

Kerans, C., & Tinker, S. W. (1999). Extrinsic stratigraphic controls on development of the Capitan Reef Complex. In A. H. Saller, P. M. Harris, B. L. Kirkland, & S. J. Mazzullo (Eds.), *Geologic Framework of the Capitan Reef*. Tulsa, Oklahoma: SEPM (Society for Sedimentary Geology).

Kolonic, S., Wagner, T., Forster, A., Sinninghe Damsté, J. S., Walsworth-Bell, B., Erba, E., et al. (2005). Black shale deposition on the northwest African Shelf during the Cenomanian/Turonian oceanic anoxic event: Climate coupling and global organic carbon burial: BLACK SHALE DEPOSITION DURING THE CENOMA. *Paleoceanography*, *20*(1), n/a-n/a. https://doi.org/10.1029/2003PA000950

Korte, C., Kozur, H., Joachimski, M., Strauss, H., Veizer, J., & Schwark, L. (2004). Carbon, sulfur, oxygen and strontium isotope records, organic geochemistry and biostratigraphy across the Permian/Triassic boundary in Abadeh, Iran. *International Journal of Earth Sciences*, *93*(4), 565–581. https://doi.org/10.1007/s00531-004-0406-7

Kozik, N. P., Young, S. A., Bowman, C. N., Saltzman, M. R., & Them, T. R. (2019). Middle–Upper Ordovician (Darriwilian–Sandbian) paired carbon and sulfur isotope stratigraphy from the Appalachian Basin, USA: Implications for dynamic redox conditions spanning the peak of the Great Ordovician Biodiversification Event. *Palaeogeography, Palaeoclimatology, Palaeoecology*, *520*, 188–202. https://doi.org/10.1016/j.palaeo.2019.01.032

Kramm, U., & Wedepohl, K. H. (1991). The isotopic composition of strontium and sulfur in seawater of Late Permian (Zechstein) age. *Chemical Geology*, *90*(3), 253–262. https://doi.org/10.1016/0009-2541(91)90103-X

Kump, L. R., & Garrels, R. M. (1986). Modeling atmospheric O 2 in the global sedimentary redox cycle. *American Journal of Science*, *286*(5), 337–360. https://doi.org/10.2475/ajs.286.5.337

Kurtz, A. C., Kump, L. R., Arthur, M. A., Zachos, J. C., & Paytan, A. (2003). Early Cenozoic decoupling of the global carbon and sulfur cycles. *Paleoceanography*, *18*(4), 1090. https://doi.org/10.1029/2003PA000908

Lark, R. M., & Webster, R. (2006). Geostatistical mapping of geomorphic variables in the presence of trend. *Earth Surface Processes and Landforms*, *31*(7), 862–874. https://doi.org/10.1002/esp.1296

Li, P., Huang, J., Chen, M., & Bai, X. (2009). Coincident negative shifts in sulfur and carbon isotope compositions prior to the end-Permian mass extinction at Shangsi Section of Guangyuan, South China. *Frontiers of Earth Science in China*, *3*(1), 51–56. https://doi.org/10.1007/s11707-009-0018-4

Longinelli, A., & Flora, O. (2007). Isotopic composition of gypsum samples of Permian and Triassic age from the north-eastern Italian Alps: Palaeoenvironmental implications. *Chemical Geology*, *245*(3), 275–284. https://doi.org/10.1016/j.chemgeo.2007.08.009

Loprieno, A., Bousquet, R., Bucher, S., Ceriani, S., Dalla Torre, F. H., Fügenschuh, B., & Schmid, S. M. (2011). The Valais units in Savoy (France): a key area for understanding the palaeogeography and the tectonic evolution of the Western Alps. *International Journal of Earth Sciences*, *100*(5), 963–992. https://doi.org/10.1007/s00531-010-0595-1

Lowenstein, T. K., Hardie, L. A., Timofeeff, M. N., & Demicco, R. V. (2003). Secular variation in seawater chemistry and the origin of calcium chloride basinal brines. *Geology*, *31*(10), 857–860. https://doi.org/10.1130/G19728r.1

Loyd, S. J., Marenco, P. J., Hagadorn, J. W., Lyons, T. W., Kaufman, A. J., Sour-Tovar, F., & Corsetti, F. A. (2012). Sustained low marine sulfate concentrations from the Neoproterozoic to the Cambrian: Insights from carbonates of northwestern Mexico and eastern California. *Earth and Planetary Science Letters*, *339–340*(0), 79–94. https://doi.org/10.1016/j.epsl.2012.05.032

Lu, F. H., & Meyers, W. J. (2003). Sr, S, and OSO4 Isotopes and the Depositional Environments of the Upper Miocene Evaporites, Spain. *Journal of Sedimentary Research*, *73*(3), 444–450. https://doi.org/10.1306/093002730444

Luo, G., Kump, L. R., Wang, Y., Tong, J., Arthur, M. A., Yang, H., et al. (2010). Isotopic evidence for an anomalously low oceanic sulfate concentration following end-Permian mass extinction. *Earth and Planetary Science Letters*, *300*(1–2), 101–111. https://doi.org/10.1016/j.epsl.2010.09.041

Lyons, T. W., Walter, L. M., Gellatly, A. M., Martini, A. M., & Blake, R. E. (2004). Sites of anomalous organic remineralization in the carbonate sediments of South Florida, USA: The sulfur cycle and carbonate-associated sulfate. In J. P. Amend, K. J. Edwards, & T. W. Lyons (Eds.), *Sulfur Biogeochemistry - Past and Present* (pp. 161–176). Boulder, Colorado: Geological Society of America.

Lyu, Z., Zhang, L., Algeo, T. J., Zhao, L., Chen, Z.-Q., Li, C., et al. (2019). Global-ocean circulation changes during the Smithian–Spathian transition inferred from carbon-sulfur cycle records. *Earth-Science Reviews*. https://doi.org/10.1016/j.earscirev.2019.01.010

Maharjan, D., Jiang, G., Peng, Y., & Nicholl, M. J. (2018). Sulfur isotope change across the Early Mississippian K–O (Kinderhookian–Osagean) δ 13 C excursion. *Earth and Planetary Science Letters*, *494*, 202–215. https://doi.org/10.1016/j.epsl.2018.04.043

Marenco, P. J., Corsetti, F. A., Kaufman, A. J., & Bottjer, D. J. (2008). Environmental and diagenetic variations in carbonate associated sulfate: An investigation of CAS in the Lower Triassic of the western USA. *Geochimica et Cosmochimica Acta*, *72*, 1570–1582.

Marenco, P. J., Corsetti, F. A., Hammond, D. E., Kaufman, A. J., & Bottjer, D. J. (2008). Oxidation of pyrite during extraction of carbonate associated sulfate. *Chemical Geology*, *247*, 124–132.

Marenco, Pedro J., Marenco, K. N., Lubitz, R. L., & Niu, D. (2013). Contrasting long-term global and short-term local redox proxies during the Great Ordovician Biodiversification Event: A case study from Fossil Mountain, Utah, USA. *Palaeogeography, Palaeoclimatology, Palaeoecology*, *377*, 45–51. https://doi.org/10.1016/j.palaeo.2013.03.007

Marenco, Pedro J., Martin, K. R., Marenco, K. N., & Barber, D. C. (2016). Increasing global ocean oxygenation and the Ordovician Radiation: Insights from Th/U of carbonates from the Ordovician of western Utah. *Palaeogeography, Palaeoclimatology, Palaeoecology*, *458*, 77–84. https://doi.org/10.1016/j.palaeo.2016.05.014

Martin, E. E., & Scher, H. D. (2004). Preservation of seawater Sr and Nd isotopes in fossil fish teeth: bad news and good news. *Earth and Planetary Science Letters*, *220*(1), 25–39. https://doi.org/10.1016/S0012-821X(04)00030-5

Mazzullo, S. J. (1982). Stratigraphy and Depositional Mosaics of Lower Clear Fork and Wichita Groups (Permian), Northern Midland Basin, Texas. *AAPG Bulletin*, *66*(2), 210–227. https://doi.org/10.1306/03B59A67-16D1-11D7-8645000102C1865D

Mekhtiyeva, V. (1974). Sulfur isotopic composition of fossil molluscan shells as an indicator of hydrochemical conditions in ancient basins. *Geochemistry International*, *11*, 1188–1192.

Meng, F.-W., Zhang, Z., Yan, X., Ni, P., Liu, W.-H., Fan, F., & Xie, G.-W. (2019). Stromatolites in Middle Ordovician carbonate–evaporite sequences and their carbon and sulfur isotopes stratigraphy, Ordos Basin, northwestern China. *Carbonates and Evaporites*, *34*(1), 11–20. https://doi.org/10.1007/s13146-017-0367-0

Meng, F.-W., Zhang, Z., Schiffbauer, J. D., Zhuo, Q., Zhao, M., Ni, P., et al. (2019). The Yudomski event and subsequent decline: new evidence from δ34S data of lower and middle Cambrian evaporites in the Tarim Basin, western China. *Carbonates and Evaporites*, *34*(3), 1117–1129. https://doi.org/10.1007/s13146-017-0407-9

Meyers Stephen R., Sageman Bradley B., & Arthur Michael A. (2012). Obliquity forcing of organic matter accumulation during Oceanic Anoxic Event 2. *Paleoceanography*, *27*(3). https://doi.org/10.1029/2012PA002286

Mills, J. V., Gomes, M. L., Kristall, B., Sageman, B. B., Jacobson, A. D., & Hurtgen, M. T. (2017). Massive volcanism, evaporite deposition, and the chemical evolution of the Early Cretaceous ocean. *Geology*, *45*(5), 475–478. https://doi.org/10.1130/G38667.1

Murray, S. T., Higgins, J. A., Holmden, C., Lu, C., & Swart, P. K. (2020). Geochemical fingerprints of dolomitization in Bahamian carbonates: Evidence from sulphur, calcium, magnesium and clumped isotopes. *Sedimentology*. https://doi.org/10.1111/sed.12775

Newton, R. J., Pevitt, E. L., Wignall, P. B., & Bottrell, S. H. (2004). Large shifts in the isotopic composition of seawater sulphate across the Permo–Triassic boundary in northern Italy. *Earth and Planetary Science Letters*, *218*, 331–345. https://doi.org/10.1016/S0012-821X(03)00676-9

Newton, R. J., Reeves, E. P., Kafousia, N., Wignall, P. B., Bottrell, S. H., & Sha, J. (2011). Low marine sulfate concentrations and the isolation of the European epicontinental sea during the Early Jurassic. *Geology*, *39*, 7–10. https://doi.org/10.1130/g31326.1

Nielsen, H. (1989). Local and global aspects of the sulphur isotope age curve of oceanic sulphate. *Evolution of the Global Biogeochemical Sulphur Cycle. Wiley, New York*, 57–64.

Nielsen, H., & Ricke, W. (1964). Schwefel-isotopen verhältnisse von evaporiten aus deutschland; Ein beitrag zur kenntnis von δ34S im meerwasser-sulfat. *Geochimica et Cosmochimica Acta*, *28*(5), 577–591. https://doi.org/10.1016/0016-7037(64)90078-X

Novikov, D. A. (2017). Distribution of Cambrian salts in the western Siberian craton (Yurubcheno-Tokhomo field, Russia). *Arabian Journal of Geosciences*, *10*(1). https://doi.org/10.1007/s12517-016-2792-0

Ohkouchi, N., Kawamura, K., Kajiwara, Y., Wada, E., Okada, M., Kanamatsu, T., & Taira, A. (1999). Sulfur isotope records around Livello Bonarelli (northern Apennines, Italy) black shale at the Cenomanian-Turonian boundary. *Geology*, *27*, 535–538. https://doi.org/10.1130/0091-7613(1999)027<0535:siralb>2.3.co;2

Owens, J. D., Gill, B. C., Jenkyns, H. C., Bates, S. M., Severmann, S., Kuypers, M. M. M., et al. (2013). Sulfur isotopes track the global extent and dynamics of euxinia during Cretaceous Oceanic Anoxic Event 2. *Proceedings of the National Academy of Sciences*, *110*(46), 18407–18412. https://doi.org/10.1073/pnas.1305304110

Pankina, R. G., Maksimov, S. P., Kalinko, M. K., Monakhov, I. B., & Guriyeva, S. M. (1975). Sulfur isotopic composition in the Phanerozoic evaporites of Bulgaria. *Geochemistry International*, *12*(6), 79–83.

Paris, G., Sessions, A. L., Subhas, A. V., & Adkins, J. F. (2013). MC-ICP-MS measurement of δ34S and Δ33S in small amounts of dissolved sulfate. *Chemical Geology*, *345*, 50–61. https://doi.org/10.1016/j.chemgeo.2013.02.022

Paris, G., Fehrenbacher, J. S., Sessions, A. L., Spero, H. J., & Adkins, J. F. (2014). Experimental determination of carbonate-associated sulfate δ34S in planktonic foraminifera shells. *Geochemistry, Geophysics, Geosystems*, *15*(4), 1452–1461. https://doi.org/10.1002/2014GC005295

Paris, G., Adkins, J. F., Sessions, A. L., Webb, S. M., & Fischer, W. W. (2014). Neoarchean carbonate–associated sulfate records positive Δ33S anomalies. *Science*, *346*(6210), 739–741. https://doi.org/10.1126/science.1258211

Paytan, A., Kastner, M., Martin, E. E., Macdougall, J. D., & Herbert, T. (1993). Marine barite as a monitor of seawater strontium isotope composition. *Nature*, *366*, 445–449.

Paytan, A., Kastner, M., Campbell, D., & Thiemens, M. H. (1998). Sulfur Isotopic Composition of Cenozoic Seawater Sulfate. *Science*, *282*, 1459–1462. https://doi.org/10.1126/science.282.5393.1459

Paytan, A., Mearon, S., Cobb, K., & Kastner, M. (2002). Origin of marine barite deposits: Sr and S isotope characterization. *Geology*, *30*, 747–750. https://doi.org/10.1130/0091-7613(2002)030<0747:oombds>2.0.co;2

Paytan, A., Kastner, M., Campbell, D., & Thiemens, M. H. (2004). Seawater Sulfur Isotope Fluctuations in the Cretaceous. *Science*, *304*, 1663–1665. https://doi.org/10.1126/science.1095258

Peryt, T. M., Halas, S., & Hryniv, S. P. (2010). Sulphur and oxygen isotope signatures of late Permian Zechstein anhydrites, West Poland: seawater evolution and diagenetic constraints. *Geological Quarterly*, *54*, 387–400.

Pisarchik, Y. K., & Golubchina, M. N. (1975). On isotope ratios of sulfur in the Cambrian sulfatic limestones of the Siberian platform. *Geochemistry International*, *12*, 227–230.

Playà, E., Cendón, D. I., Travé, A., Chivas, A. R., & García, A. (2007). Non-marine evaporites with both inherited marine and continental signatures: The Gulf of Carpentaria, Australia, at ∼70 ka. *Sedimentary Geology*, *201*(3–4), 267–285. https://doi.org/10.1016/j.sedgeo.2007.05.010

Pope, M. C., & Grotzinger, J. P. (2003). Paleoproterozoic Stark Formation, Athapuscow Basin, Northwest Canada: Record of Cratonic-Scale Salinity Crisis. *Journal of Sedimentary Research*, *73*(2), 280–295. https://doi.org/10.1306/091302730280

Posey, H. H., & Fisher, S. R. (1989). A sulfur and strontium isotopic investigation of Lower Permian anhydrite, Palo Duro Basin, Texas, U.S.A. *Applied Geochemistry*, *4*(4), 395–407. https://doi.org/10.1016/0883-2927(89)90015-2

Poulton, S. W., Henkel, S., März, C., Urquhart, H., Flögel, S., Kasten, S., et al. (2015). A continental-weathering control on orbitally driven redox-nutrient cycling during Cretaceous Oceanic Anoxic Event 2. *Geology*, *43*(11), 963–966. https://doi.org/10.1130/G36837.1

Present, T. M. (2018). *Controls on the Sulfur Isotopic Composition of Carbonate-Associated Sulfate* (Ph.D.). California Institute of Technology, Pasadena, California. Retrieved from http://resolver.caltech.edu/CaltechTHESIS:04042018-153105432

Present, T. M., Paris, G., Burke, A., Fischer, W. W., & Adkins, J. F. (2015). Large Carbonate Associated Sulfate isotopic variability between brachiopods, micrite, and other sedimentary components in Late Ordovician strata. *Earth and Planetary Science Letters*, *432*, 187–198. https://doi.org/10.1016/j.epsl.2015.10.005

Present, T. M., Gutierrez, M., Paris, G., Kerans, C., Grotzinger, J. P., & Adkins, J. F. (2019). Diagenetic controls on the isotopic composition of carbonate-associated sulphate in the Permian Capitan Reef Complex, West Texas. *Sedimentology*, *66*(7), 2605–2626. https://doi.org/10.1111/sed.12615

Prokoph, A., Shields, G. A., & Veizer, J. (2008). Compilation and time-series analysis of a marine carbonate δ18O, δ13C, 87Sr/86Sr and δ34S database through Earth history. *Earth-Science Reviews*, *87*(3–4), 113–133. https://doi.org/10.1016/j.earscirev.2007.12.003

Qiu, Z., Sun, S., Wei, H., Wang, Q., Zou, C., & Zhang, Y. (2015). SIMS zircon U-Pb dating from bentonites in the Penglaitan Global Stratotype Section for the Guadalupian–Lopingian boundary (GLB), South China. *Geological Journal*.

Raab, M., & Spiro, B. (1991). Sulfur isotopic variations during seawater evaporation with fractional crystallization. *Chemical Geology: Isotope Geoscience Section*, *86*(4), 323–333. https://doi.org/10.1016/0168-9622(91)90014-N

Rennie, V. C. F., & Turchyn, A. V. (2014). The preservation of d34SSO4 and d18OSO4 in carbonate-associated sulfate during marine diagenesis: A 25 Myr test case using marine sediments. *Earth and Planetary Science Letters*, *395*, 13–23. https://doi.org/10.1016/j.epsl.2014.03.025

Rennie, V. C. F., Paris, G., Sessions, A. L., Abramovich, S., Turchyn, A. V., & Adkins, J. F. (2018). Cenozoic record of δ 34 S in foraminiferal calcite implies an early Eocene shift to deep-ocean sulfide burial. *Nature Geoscience*, (11), 761–765. https://doi.org/10.1038/s41561-018-0200-y

Riccardi, A. L., Arthur, M. A., & Kump, L. R. (2006). Sulfur isotopic evidence for chemocline upward excursions during the end-Permian mass extinction. *Geochimica et Cosmochimica Acta*, *70*, 5740–5752.

Richardson, J. A., Newville, M., Lanzirotti, A., Webb, S. M., Rose, C. V., Catalano, J. G., & Fike, D. A. (2019). Depositional and diagenetic constraints on the abundance and spatial variability of carbonate-associated sulfate. *Chemical Geology*, *523*, 59–72. https://doi.org/10.1016/j.chemgeo.2019.05.036

Richardson, J. A., Keating, C., Lepland, A., Hints, O., Bradley, A. S., & Fike, D. A. (2019). Silurian records of carbon and sulfur cycling from Estonia: The importance of depositional environment on isotopic trends. *Earth and Planetary Science Letters*, *512*, 71–82. https://doi.org/10.1016/j.epsl.2019.01.055

Rine, M. J., Garrett, J. D., & Kaczmarek, S. E. (2017). A New Facies Architecture Model for the Silurian Niagaran Pinnacle Reef Complexes of the Michigan Basin. In A. J. Macneil, J. Lonnee, & R. Wood, *Characterization and Modeling of Carbonates–Mountjoy Symposium 1*. SEPM (Society for Sedimentary Geology). https://doi.org/10.2110/sepmsp.109.02

Rose, C. V., Fischer, W. W., Finnegan, S., & Fike, D. A. (2019). Records of carbon and sulfur cycling during the Silurian Ireviken Event in Gotland, Sweden. *Geochimica et Cosmochimica Acta*, *246*, 299–316. https://doi.org/10.1016/j.gca.2018.11.030

Sakai, H. (1972). Oxygen isotopic ratios of some evaporites from Precambrian to Recent ages. *Earth and Planetary Science Letters*, *15*(2), 201–205. https://doi.org/10.1016/0012-821X(72)90061-1

Saltzman, M. R., Cowan, C. A., Runkel, A. C., Runnegar, B., Stewart, M. C., & Palmer, A. R. (2004). The Late Cambrian Spice (δ13C) Event and the Sauk II-SAUK III Regression: New Evidence from Laurentian Basins in Utah, Iowa, and Newfoundland. *Journal of Sedimentary Research*, *74*(3), 366–377. https://doi.org/10.1306/120203740366

Saltzman, M. R., Edwards, C. T., Adrain, J. M., & Westrop, S. R. (2015). Persistent oceanic anoxia and elevated extinction rates separate the Cambrian and Ordovician radiations. *Geology*, *43*(9), 807–810. https://doi.org/10.1130/g36814.1

Schobben, M., Stebbins, A., Ghaderi, A., Strauss, H., Korn, D., & Korte, C. (2015). Flourishing ocean drives the end-Permian marine mass extinction. *Proceedings of the National Academy of Sciences*, *112*(33), 10298–10303. https://doi.org/10.1073/pnas.1503755112

Schobben, M., Stebbins, A., Algeo, T. J., Strauss, H., Leda, L., Haas, J., et al. (2017). Volatile earliest Triassic sulfur cycle: A consequence of persistent low seawater sulfate concentrations and a high sulfur cycle turnover rate? *Palaeogeography, Palaeoclimatology, Palaeoecology*, *486*, 74–85. https://doi.org/10.1016/j.palaeo.2017.02.025

Schrag, D. P., DePaolo, D. J., & Richter, F. M. (1995). Reconstructing past sea surface temperatures: Correcting for diagenesis of bulk marine carbonate. *Geochimica et Cosmochimica Acta*, *59*(11), 2265–2278. https://doi.org/10.1016/0016-7037(95)00105-9

Schröder, S., Schreiber, B. C., Amthor, J. E., & Matter, A. (2004). Stratigraphy and environmental conditions of the terminal Neoproterozoic–Cambrian Period in Oman: evidence from sulphur isotopes. *Journal of the Geological Society*, *161*(3), 489–499. https://doi.org/10.1144/0016-764902-062

Sim, M. S., Bosak, T., & Ono, S. (2011). Large Sulfur Isotope Fractionation Does Not Require Disproportionation. *Science*, *333*(6038), 74–77. https://doi.org/10.1126/science.1205103

Sim, M. S., Ono, S., & Hurtgen, M. T. (2015). Sulfur isotope evidence for low and fluctuating sulfate levels in the Late Devonian ocean and the potential link with the mass extinction event. *Earth and Planetary Science Letters*, *419*, 52–62. https://doi.org/10.1016/j.epsl.2015.03.009

Solomon, M., Rafter, T. A., & Dunham, K. C. (1971). Sulphur and oxygen isotope studies in the northern Pennines in relation to ore genesis. *Transactions of the Institution of Mining and Metallurgy Section B*, *80B*, 259–275.

Song, H., Tong, J., Algeo, T. J., Song, H., Qiu, H., Zhu, Y., et al. (2014). Early Triassic seawater sulfate drawdown. *Geochimica et Cosmochimica Acta*, *128*(0), 95–113. https://doi.org/10.1016/j.gca.2013.12.009

Song, H., Du, Y., Algeo, T. J., Tong, J., Owens, J. D., Song, H., et al. (2019). Cooling-driven oceanic anoxia across the Smithian/Spathian boundary (mid-Early Triassic). *Earth-Science Reviews*. https://doi.org/10.1016/j.earscirev.2019.01.009

Spötl, C. (1988). Schwefelisotopendatierungen und fazielle Entwicklung permoskytischer Anhydrite in den Salzbergbauen von Dürrnberg/Hallstein und Hallstadt (Österreich). *Mitteilungen Der Gesellschaft Der Geologie- Und Bergbaustudenten in Österreich*, *34–35*, 209–229.

Staudt, W. J., & Schoonen, M. A. A. (1995). Sulfate Incorporation into Sedimentary Carbonates. In *Geochemical Transformations of Sedimentary Sulfur* (Vol. 612, pp. 332–345). American Chemical Society. https://doi.org/10.1021/bk-1995-0612.ch018

Stebbins, A., Algeo, T. J., Krystyn, L., Rowe, H., Brookfield, M., Williams, J., et al. (2019). Marine sulfur cycle evidence for upwelling and eutrophic stresses during Early Triassic cooling events. *Earth-Science Reviews*. https://doi.org/10.1016/j.earscirev.2018.09.007

Stollhofen, H., Bachmann, G. H., Barnasch, J., Bayer, U., Beutler, G., Franz, M., et al. (2008). Upper Rotliegend to early cretaceous basin development. *Dynamics of Complex Intracontinental Basins. The Central European Basin System*, 181–210.

Strauss, H. (1997). The isotopic composition of sedimentary sulfur through time. *Palaeogeography, Palaeoclimatology, Palaeoecology*, *132*, 97–118. https://doi.org/10.1016/s0031-0182(97)00067-9

Taki, H. E., & Pratt, B. R. (2012). Syndepositional tectonic activity in an epicontinental basin revealed by deformation of subaqueous carbonate laminites and evaporites: Seismites in Red River strata (Upper Ordovician) of southern Saskatchewan, Canada. *Bulletin of Canadian Petroleum Geology*, *60*(1), 37–58. https://doi.org/10.2113/gscpgbull.60.1.37

Theiling, B. P., & Coleman, M. (2015). Refining the extraction methodology of carbonate associated sulfate: Evidence from synthetic and natural carbonate samples. *Chemical Geology*, *411*, 36–48. https://doi.org/10.1016/j.chemgeo.2015.06.018

Thode, H. G., & Monster, J. (1965). Sulfur-Isotope Geochemistry of Petroleum, Evaporites, and Ancient Seas. In A. Young & J. E. Galley (Eds.), *AAPG Memoir 4: Fluids in subsurface environments* (Vol. 71, pp. 367–377). Tulsa, Oklahoma: American Association of Petroleum Geologists. Retrieved from http://archives.datapages.com/data/specpubs/methodo2/data/a071/a071/0001/0350/0367.htm

Thode, H. G., & Monster, J. (1970). Sulfur Isotope Abundances and Genetic Relations of Oil Accumulations in Middle East Basin. *AAPG Bulletin*, *54*(4), 627–637.

Thode, H. G., Macnamara, J., & Fleming, W. H. (1953). Sulphur isotope fractionation in nature and geological and biological time scales. *Geochimica et Cosmochimica Acta*, *3*(5), 235–243. https://doi.org/10.1016/0016-7037(53)90042-8

Thode, H. G., Monster, J., & Dunford, H. B. (1958). Sulphur Isotope Abundances in Petroleum and Associated Materials. *AAPG Bulletin*, *42*(11), 2619–2641.

Thompson, Cara K., & Kah, L. C. (2012). Sulfur isotope evidence for widespread euxinia and a fluctuating oxycline in Early to Middle Ordovician greenhouse oceans. *Palaeogeography, Palaeoclimatology, Palaeoecology*, *313–314*(0), 189–214. https://doi.org/10.1016/j.palaeo.2011.10.020

Thompson, Cara K., Kah, L. C., Astini, R., Bowring, S. A., & Buchwaldt, R. (2012). Bentonite geochronology, marine geochemistry, and the Great Ordovician Biodiversification Event (GOBE). *Palaeogeography, Palaeoclimatology, Palaeoecology*, *321–322*(0), 88–101. https://doi.org/10.1016/j.palaeo.2012.01.022

Thompson, Cara Kim. (2011). *Carbon and Sulfur Cycling in Early Paleozoic Oceans* (Ph.D. diss). University of Tennessee, Knoxville.

Toggweiler, J. R., & Sarmiento, J. L. (1985). Glacial to Interglacial Changes in Atmospheric Carbon Dioxide: The Critical Role of Ocean Surface Water in High Latitudes. In *The Carbon Cycle and Atmospheric CO2: Natural Variations Archean to Present* (pp. 163–184). American Geophysical Union (AGU). https://doi.org/10.1029/GM032p0163

Torres, M. A., West, A. J., & Li, G. (2014). Sulphide oxidation and carbonate dissolution as a source of CO_2 over geological timescales. *Nature*, *507*(7492), 346–349. https://doi.org/10.1038/nature13030

Torres, M. E., Brumsack, H. J., Bohrmann, G., & Emeis, K. C. (1996). Barite fronts in continental margin sediments: a new look at barium remobilization in the zone of sulfate reduction and formation of heavy barites in diagenetic fronts. *Chemical Geology*, *127*, 125–139. https://doi.org/10.1016/0009-2541(95)00090-9

Turchyn, A. V., & DePaolo, D. J. (2019). Seawater Chemistry Through Phanerozoic Time. *Annual Review of Earth and Planetary Sciences*, *47*(1), 197–224. https://doi.org/10.1146/annurev-earth-082517-010305

Turchyn, A. V., Schrag, D. P., Coccioni, R., & Montanari, A. (2009). Stable isotope analysis of the Cretaceous sulfur cycle. *Earth and Planetary Science Letters*, *285*, 115–123. https://doi.org/10.1016/j.epsl.2009.06.002

Utrilla, R., Pierre, C., Orti, F., & Pueyo, J. J. (1992). Oxygen and sulphur isotope compositions as indicators of the origin of Mesozoic and Cenozoic evaporites from Spain. *Chemical Geology*, *102*(1), 229–244. https://doi.org/10.1016/0009-2541(92)90158-2

Veizer, J., Holser, W. T., & Wilgus, C. K. (1980). Correlation of 13C12C and 34S32S secular variations. *Geochimica et Cosmochimica Acta*, *44*(4), 579–587. https://doi.org/10.1016/0016-7037(80)90250-1

Vinogradov, V. I. (2007). Was there a conflict at the Neoproterozoic-Cambrian boundary: Evidence from sulfur isotope composition? *Lithology and Mineral Resources*, *42*(1), 1–14. https://doi.org/10.1134/S0024490207010014

Voigt, S., Erbacher, J., Mutterlose, J., Weiss, W., Westerhold, T., Wiese, F., et al. (2008). The Cenomanian – Turonian of the Wunstorf section – (North Germany): global stratigraphic reference section and new orbital time scale for Oceanic Anoxic Event 2. *Newsletters on Stratigraphy*, *43*(1), 65–89. https://doi.org/10.1127/0078-0421/2008/0043-0065

Vredenburgh, L. D., & Cheney, E. S. (1971). Sulfur and carbon isotopic investigation of petroleum, Wind River basin, Wyoming. *AAPG Bulletin*, *55*(11), 1954–1975.

Walker, J. C. (1986). Global geochemical cycles of carbon, sulfur and oxygen. *Marine Geology*, *70*(1), 159–174.

Warren, J. K. (2010). Evaporites through time: Tectonic, climatic and eustatic controls in marine and nonmarine deposits. *Earth-Science Reviews*, *98*(3), 217–268. https://doi.org/10.1016/j.earscirev.2009.11.004

Webster, R., & Oliver, M. A. (2007). *Geostatistics for environmental scientists* (2nd ed.). Chichester, UK: Wiley.

Wei, W., & Gartner, S. (1993). 2. Neogene Calcareous Nannofossils from Sites 811 and 819 Through 825, offshore Northeastern Australia. In J. A. McKenzie, P. J. Davies, & A. Palmer-Julson (Eds.), *Scientific Results* (Vol. 133, pp. 19–37). College Station, Texas: Ocean Drilling Program. https://doi.org/10.2973/odp.proc.sr.133.1993

Westerhold, T., Röhl, U., Raffi, I., Fornaciari, E., Monechi, S., Reale, V., et al. (2008). Astronomical calibration of the Paleocene time. *Palaeogeography, Palaeoclimatology, Palaeoecology*, *257*(4), 377–403. https://doi.org/10.1016/j.palaeo.2007.09.016

Witts, J. D., Newton, R. J., Mills, B. J. W., Wignall, P. B., Bottrell, S. H., Hall, J. L. O., et al. (2018). The impact of the Cretaceous–Paleogene (K–Pg) mass extinction event on the global sulfur cycle: Evidence from Seymour Island, Antarctica. *Geochimica et Cosmochimica Acta*. https://doi.org/10.1016/j.gca.2018.02.037

Worden, R. H., Smalley, P. C., & Fallick, A. E. (1997). Sulfur cycle in buried evaporites. *Geology*, *25*(7), 643–646. https://doi.org/10.1130/0091-7613(1997)025<0643:SCIBE>2.3.CO;2

Wotte, T., Strauss, H., & Sundberg, F. A. (2011). Carbon and Sulfur Isotopes from the Cambrian Series 2-Cambrian Series 3 of Laurentia and Siberia. In J. S. Hollingsworth, F. A. Sundberg, & J. R. Foster (Eds.), *Museum of Northern Arizona Bulletin 67: Cambrian Stratigraphy and Paleontology of Northern Arizona and Southern Nevada: The 16th Field Conference of the Cambrian Stage Subdivision Working Group, International Subcommission on Cambrian Stratigraphy, Flagstaff, Arizona, and Southern Nevada, United States* (pp. 43–63). Flagstaff, Arizona: Museum of Northern Arizona.

Wotte, T., Shields-Zhou, G. A., & Strauss, H. (2012). Carbonate-associated sulfate: Experimental comparisons of common extraction methods and recommendations toward a standard analytical protocol. *Chemical Geology*, *326–327*, 132–144. https://doi.org/10.1016/j.chemgeo.2012.07.020

Wright, J. D., & Kroon, D. (2000). Planktonic foraminiferal biostratigraphy of Leg 166. In P. K. Swart, G. P. Eberli, M. J. Malone, & J. F. Sarg (Eds.), *Scientific Results* (Vol. 166, pp. 3–12). College Station, Texas: Ocean Drilling Program. https://doi.org/10.2973/odp.proc.sr.166.2000

Wu, N. (2013). *Sulfur isotopic evolution of Phanerozoic and Ediacaran seawater sulfate*. University of Maryland, College Park, Md. Retrieved from http://hdl.handle.net/1903/14016

Wu, N., Farquhar, J., Strauss, H., Kim, S.-T., & Canfield, D. E. (2010). Evaluating the S-isotope fractionation associated with Phanerozoic pyrite burial. *Geochimica et Cosmochimica Acta*, *74*(7), 2053–2071. https://doi.org/10.1016/j.gca.2009.12.012

Wu, N., Farquhar, J., & Strauss, H. (2014). δ34S and Δ33S records of Paleozoic seawater sulfate based on the analysis of carbonate associated sulfate. *Earth and Planetary Science Letters*, *399*(0), 44–51. https://doi.org/10.1016/j.epsl.2014.05.004

Wu, Q., Ramezani, J., Zhang, H., Yuan, D., Erwin, D. H., Henderson, C. M., et al. (2020). High-precision U-Pb zircon age constraints on the Guadalupian in West Texas, USA. *Palaeogeography, Palaeoclimatology, Palaeoecology*, *548*, 109668. https://doi.org/10.1016/j.palaeo.2020.109668

Yadong, S., Xulong, L., Haishui, J., Genming, L., Si, S., Chunbo, Y., & Wignall, P. B. (2008). Guadalupian (Middle Permian) Conodont Faunas at Shangsi Section, Northeast Sichuan Province. *Journal of China University of Geosciences*, *19*(5), 451–460. https://doi.org/10.1016/S1002-0705(08)60050-3

Yan, D., Zhang, L., & Qiu, Z. (2013). Carbon and sulfur isotopic fluctuations associated with the end-Guadalupian mass extinction in South China. *Gondwana Research*, *24*(3–4), 1276–1282. https://doi.org/10.1016/j.gr.2013.02.008

Yang, C., Li, X.-H., Zhu, M., Condon, D. J., & Chen, J. (2018). Geochronological constraint on the Cambrian Chengjiang biota, South China. *Journal of the Geological Society*, *175*(4), 659–666. https://doi.org/10.1144/jgs2017-103

Yao, W., Paytan, A., & Wortmann, U. G. (2018). Large-scale ocean deoxygenation during the Paleocene-Eocene Thermal Maximum. *Science*, *361*(6404), 804–806. https://doi.org/10.1126/science.aar8658

Yao, W., Paytan, A., Griffith, E. M., Martínez-Ruiz, F., Markovic, S., & Wortmann, U. G. (2020). A revised seawater sulfate S-isotope curve for the Eocene. *Chemical Geology*, *532*, 119382. https://doi.org/10.1016/j.chemgeo.2019.119382

Yeremenko, N. A., & Pankina, R. G. (1972). Variations of 34S in Sulfates of Recent and Ancient Marine Basins of the Soviet Union. *Geochemistry International*, *10*, 45–54.

Young, S. A., Gill, B. C., Edwards, C. T., Saltzman, M. R., & Leslie, S. A. (2016). Middle–Late Ordovician (Darriwilian–Sandbian) decoupling of global sulfur and carbon cycles: Isotopic evidence from eastern and southern Laurentia. *Palaeogeography, Palaeoclimatology, Palaeoecology*, *458*, 118–132. https://doi.org/10.1016/j.palaeo.2015.09.040

Young, S. A., Kleinberg, A., & Owens, J. D. (2019). Geochemical evidence for expansion of marine euxinia during an early Silurian (Llandovery–Wenlock boundary) mass extinction. *Earth and Planetary Science Letters*, *513*, 187–196. https://doi.org/10.1016/j.epsl.2019.02.023

Zhang, L., Zhao, L., Chen, Z.-Q., Algeo, T. J., Li, Y., & Cao, L. (2015). Amelioration of marine environments at the Smithian–Spathian boundary, Early Triassic. *Biogeosciences*, *12*(5), 1597–1613.

Zhu, M., Yang, A., Yuan, J., Li, G., Zhang, J., Zhao, F., et al. (2019). Cambrian integrative stratigraphy and timescale of China. *Science China Earth Sciences*, *62*(1), 25–60. https://doi.org/10.1007/s11430-017-9291-0

Supporting Information for "Variability in Records of Phanerozoic Seawater Sulfate," by T. M. Present, J. F. Adkins, and W. W. Fischer (2020).

Age assignment and data compilation

6710 $\delta^{34}S$ data of sulfate from Phanerozoic marine evaporites, bulk rock CAS, biogenic CAS, or marine barite were compiled from 108 references. Some previous evaporite $\delta^{34}S$ compilations included data from salt diapirs, secondary veins in non-sedimentary rocks, aqueous brines that had dissolved nearby evaporite-bearing formations, or brackish or non-marine depositional environments; these data were excluded from this compilation. The bulk rock CAS record contains data from sedimentary carbonate phases, although the extraction procedure employed varies between studies. The biogenic CAS record includes CAS data from brachiopods, belemnites, bivalves, and foraminifera, as well as sulfate in apatite from conodonts. Although preservation of biogenic and bulk-rock CAS was addressed in each reference, all data were included in the current compilation. Sulfur isotope data from authigenic phosphorites were not included.

For data from studies that included radiometric ages, the radiometric age model was maintained. For studies that included stage-level assignments of the lithostratigraphy, ages were assigned by linearly interpolating on stratigraphic thickness unless the reference included independent estimates of sedimentation rate. For studies that assigned ages but did not include stratigraphic data, ages were updated by linearly interpolating between the assigned ages of stage boundaries in each time scale. The $\delta^{34}S$ data and stratigraphic height or age assignment was extracted graphically from figures in references that did not tabulate data. Many evaporite deposits have substantially improved stratigraphic and age assignments since publication of their sulfur isotope data. The ages of evaporite-bearing formations have been updated using the most recent tectono-stratigraphy and/or economic exploration literature.

Histograms of the four compiled proxy datasets are shown in Supporting Figure S1, and summary statistics are reported in Supporting Table S1. Supporting Table S2 includes each data source and a description of the age model applied to the reference, with applicable citations. Supporting File *d34S_Data.xlsx* tabulates the compiled $\delta^{34}S$ data with the proxy material, assigned age, and data source.

Variography

Semivariance is the variance—per point—of the difference between equally spaced pairs of measurements (Webster & Oliver, 2007, p. 54). Variograms are functions relating semivariance to the distance between the points, called the lag. In this paper, the lag is the age difference between two samples. The empirical variogram describing the semivariance of the $\delta^{34}S$ data, γ, as a function of lag, h, is estimated for $N(h)$ pairs of data with that lag:

$$\gamma(h) = \frac{1}{2}\frac{1}{N(h)}\sum_{i=1}^{N(h)}[\delta^{34}S(t_i) - \delta^{34}S(t_i + h)]^2$$

Although the variance of pairs of data may change as a function of t, the semivariance does not. If the variance was not a function of t, then the semivariance would simply mirror the covariance (Webster & Oliver, 2007, p. 55).

Formulating variance as the square of the difference is sensitive to outliers in the data. By decreasing the order of the variogram estimator from 2 and applying a correction to maintain a normal distribution, a variogram that unweights tails on the distribution and thus is more robust to outliers is developed (Cressie & Hawkins, 1980). A variogram order of 0.5 was used here:

$$\gamma_{robust}(h) = \frac{1}{2}\frac{\left[\frac{1}{N(h)}\sum_{i=1}^{N(h)}\sqrt{|\delta^{34}S(t_i) - \delta^{34}S(t_i+h)|}\right]^4}{0.457 + \frac{0.494}{N(h)} + \frac{0.045}{N^2(h)}}$$

Empirical variograms for detrended $\delta^{34}S$ data from each proxy in each era are shown in Supporting Figure S2. Because timeseries are temporally autocorrelated, the semivariance at short lags is less than at long lags. Variograms of geologic eras have enough paired data to resolve the autocorrelation structure. The maximum variability over the domain of interest is described by the population variance, and the semivariance approaches this value over an interval called the range. The population variance is often referred to as the "sill" in geospatial analysis.

At the shortest lags, the semivariance is not zero. This uncorrelated variance represents the variability of $\delta^{34}S$ measurements unresolved by sampling. It is often referred to as the "nugget" in geospatial analysis.

The approach of semivariance to the population variance can be described with a model of the structure of the empirical variogram. For our 2-dimensional (time and $\delta^{34}S$) data, semivariance can be modelled by the overlap of two circles populated randomly following a Poisson distribution (Webster & Oliver, 2007, p. 87). This circular variogram model describes semivariance as a function of lag, h, given the range, a, sill, c, and nugget, n:

$$\gamma_{model}(h) = \begin{cases} n + c\left\{1 - \frac{2}{\pi}\cos^{-1}\left(\frac{h}{a}\right) + \frac{2h}{\pi a}\sqrt{1 - \frac{h^2}{a^2}}\right\} & \text{for } h \leq a, \\ n + c & \text{for } h > a \end{cases}$$

To fit the variogram model to the empirical variogram, we diagnosed the nugget and sill from the data and visually adjusted the range: the nugget is the empirical semivariance computed at the mean minimum time between all pairs of data, and the sill is the population variance. We only require the model to estimate uncertainty in the $\delta^{34}S$ records—we are not attempting to predict $\delta^{34}S$ compositions in rocks that haven't been sampled. Therefore, it was unnecessary to employ more agnostic strategies to select a variogram model and fit it to the empirical variogram.

Other bounded variogram models, such as spherical and exponential models, produce nearly indistinguishable results. This is because model-independent descriptions of the data—the population variance and the empirical semivariance calculated at the mean minimum lag between data—bound the minimum and maximum kriging variance. The variogram model shape and range describe the weights of data between these bounds.

Kriging

Kriging is both a method of interpolating the data and for modelling the uncertainty around the unobserved, interpolated point (Gebbers, 2010). The expected value of an interpolated point is simply a weighted average of the data. The weights are calculated using the variogram model that describes semivariance as a function of distance from observations such that the estimated semivariance of the unobserved point (called the kriging variance) is minimized.

Detrending the data is necessary to ensure that the mean is constant (first-order stationary), but results in improper estimation of total variance by failing to account for both uncertainty and bias in the detrending (Lark & Webster, 2006). Therefore, kriging variance at long lags may be underestimated (by failing to include the uncertainty of the detrending model) or even overestimated (by biased sampling affecting the detrending model and failing to capture the minimum temporal variance in that region).

We model the variogram sill as the population variance, but clear mismatches in long-lag empirical variograms are apparent (Supplemental Figure S2), with some lag intervals having both much higher and much lower variance. In addition to a violation of first-order stationarity, we interpret this as a lack of knowledge of the structure of long-term $\delta^{34}S$ trends where it is not constrained by data, rather than a quantitative statement about its variance over long timescales. In other words, dramatic sulfur isotope excursions may be possible in unsampled intervals of geologic time, and there is no predictive power from the variance deriving from the amplitude of currently observed excursions. Our goal of using the kriged variance to describe the quality of $\delta^{34}S$ records is therefore critically different than using the kriged variance to predict $\delta^{34}S$ through time, in the way that kriging is often applied to predict spatial-temporal patterns in environmental and earth sciences.

On the other hand, the estimates of uncorrelated variance—that on short timescales—are generally well constrained by the data. For estimating kriging variance through time, the variogram model at short lags is much more important than at long lags. Over the observed range of correlation until semivariance matches or exceed population variance, most records in each time interval indeed show increasing semivariance with lag distance (Supporting Figure S2). Only one set of data, the Cenozoic bulk rock CAS record, has a negligible difference between uncorrelated and population variance. Constraints on either are therefore poor, but resultant kriging variance is insensitive to the exact shape of the variogram model.

Timeseries variography and kriging of synthetic data

Variography and kriging can usefully describe the structure of variance of timeseries $\delta^{34}S$ data. In addition to differences between the proxy records inherent to each geologic archive, some variance in the records may derive from misalignment of age models.

The dashed line in Supporting Figure S3a represents a synthetic isotope excursion similar in duration and magnitude to some reported in the Paleozoic, such as during the Cambrian SPICE interval (e.g., Gill et al., 2007). The orange dots represent samples taken randomly in time from a population that follows the synthetic excursion with synthetic Gaussian noise with a standard deviation of 2‰. The variogram captures a 1‰ 1σ standard deviation of uncorrelated variance at the shortest lag interval and approaches the population variance (*ca.* 5‰) of the synthetic data over

a range of approximately 500 kyr. Applying a circular variogram model and kriging the random samples results in the gray kriged estimate.

But, given multiple aligned records, how much of the variogram structure is attributable to the inherent "noise" in the archive (illustrated in Supporting Figure S3a) and how much is attributable to poor temporal alignment? Supporting Figures S3b and S3c test this by overlaying the synthetic record in Supporting Figure S3a with randomly misaligned records. Supporting Figures S3b represents poor alignment of multiple identical records sampled at different localities by randomly misaligning the full excursion within the average length of a Paleozoic stage (5.5 Myr). Although the kriged estimate of the interpolated record and the variogram are clearly different than the true synthetic excursion, the uncorrelated variance and population variance are only slightly larger. These are robust statistical descriptions of the uncertainty in the data.

Similarly, an unconformity or uneven sedimentation rate may change the amplitude or shape of an isotope excursion if, when sampling, this is unknown. Supporting Figure S3c shows how randomly varying the amplitude of the excursion in Supporting Figure S3a with a standard deviation of 25% also does not dramatically increase the nugget or sill variance.

Uncorrelated variance's sensitivity to age misalignment is further shown in Supporting Figure S4. Different combinations of 1 to 5 synthetic records randomly misaligned with standard deviations of 1 to 10 Myr were each simulated 25 times, and the average nugget effect was calculated. This bootstrapping approach estimates the expected nugget effect solely related to poor age models. More misaligned records result in a larger nugget in the composite record, and the magnitude of the nugget is maximized if the isotope excursions are, on average, exactly out of phase (i.e., misaligned by half of the duration of the $\delta^{34}S$ excursion, modelled as 2 Myr in Supporting Figure S4).

In summary, it is likely that the increase in both uncorrelated (nugget) and population (sill) variance of all records with age represents both poorer age control in older strata, and also a meaningful change in the variability of ancient rocks due to changes in how sulfate is incorporated and preserved.

Supporting Figures, Tables, and Files

Supporting Figure S1. *Histograms of all compiled $\delta^{34}S$ data of sulfate in each proxy for ancient seawater sulfate with means and 1σ standard deviations. Arrows mark bins with 1 to 10 counts, and the broken line marks the means.*

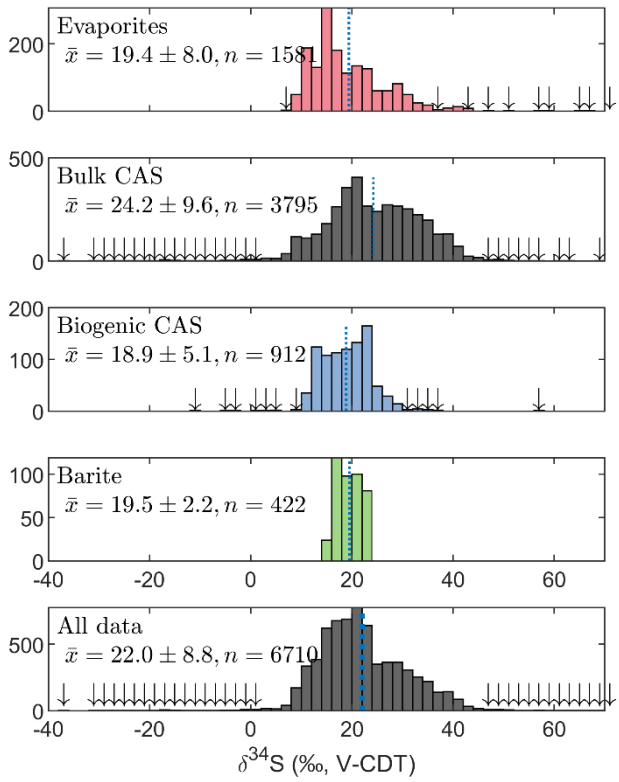

Supporting Figure S2. *Empirical variograms showing semivariance as a function of lag times less than 40 Myr for each record, and for each record by geologic age. The dashed horizontal line is the population variance of all data within the 1st and 99th percentile of the linearly detrended $\delta^{34}S$ data, which is used to estimate the sill for the circular variogram model (green solid line). The unresolved variance for each record is the semivariance at the shortest lag, computed at the mean minimum time between all pairs of data within the 1st and 99th percentile of the linearly detrended $\delta^{34}S$ data.*

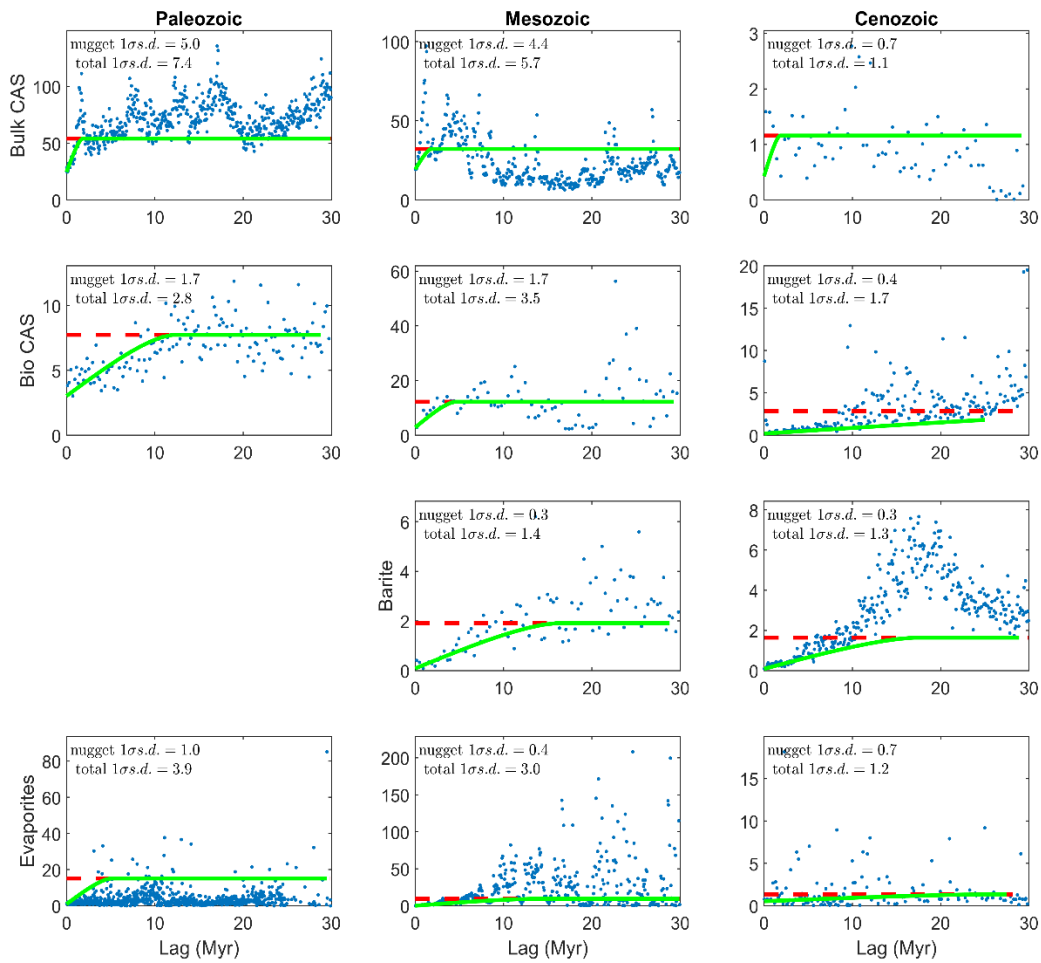

Supporting Figure S3. *Synthetic data to examine the effect sampling and age modelling on the variogram of a global isotope excursion sampled at multiple localities. All sampling and age model artifacts lead to less than 3‰ nugget effects, which may account for a source of unresolved variance in many proxy records but cannot explain all unresolved variance in the Phanerozoic.* ***(a)*** *Imprecise sampling represented by Gaussian noise with a standard deviation of 2‰ added to a synthetic* $\delta^{34}S$ *excursion with 20‰ amplitude over 2 Myr, like some Paleozoic excursions in CAS data.* ***(b)*** *Imprecise age alignment represented by precise sampling of multiple randomly aligned but otherwise identical excursions varying within the average length of a Paleozoic stratigraphic stage (standard deviation of 5.5 Myr).* ***(c)*** *Inaccurate age model represented by randomly varying amplitude with 5‰ standard deviation, which is the effect of an unconformity of unknown duration adding 25% variability to the true excursion amplitude.*

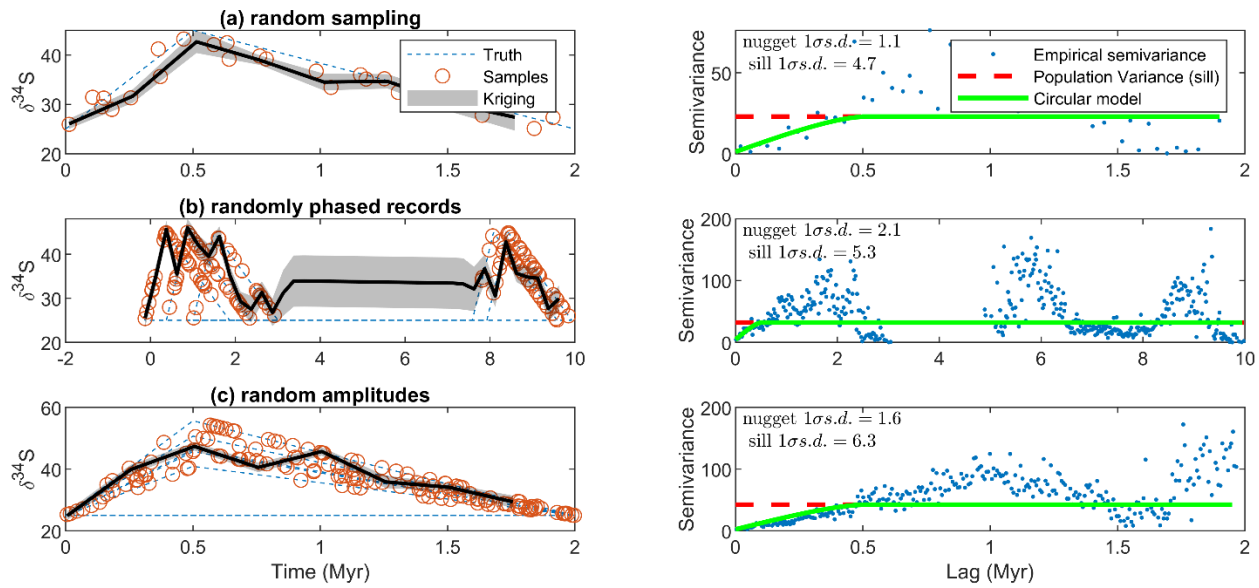

Supporting Figure S4. *Estimation of unresolved variance due to staggering multiple synthetic $\delta^{34}S$ excursions that have a duration of 2 Myr and amplitude of 20‰ (*cf. *Supporting Figure S3b). The nugget estimate is determined as the average nugget of 25 bootstrap samples of 1 to 5 synthetic excursions randomly misaligned with a standard deviation up to 5 times the length of the excursion (i.e., 10 Myr). A maximum nugget effect due to record misalignment occurs if the records are all randomly misaligned by about half of the excursion's duration.*

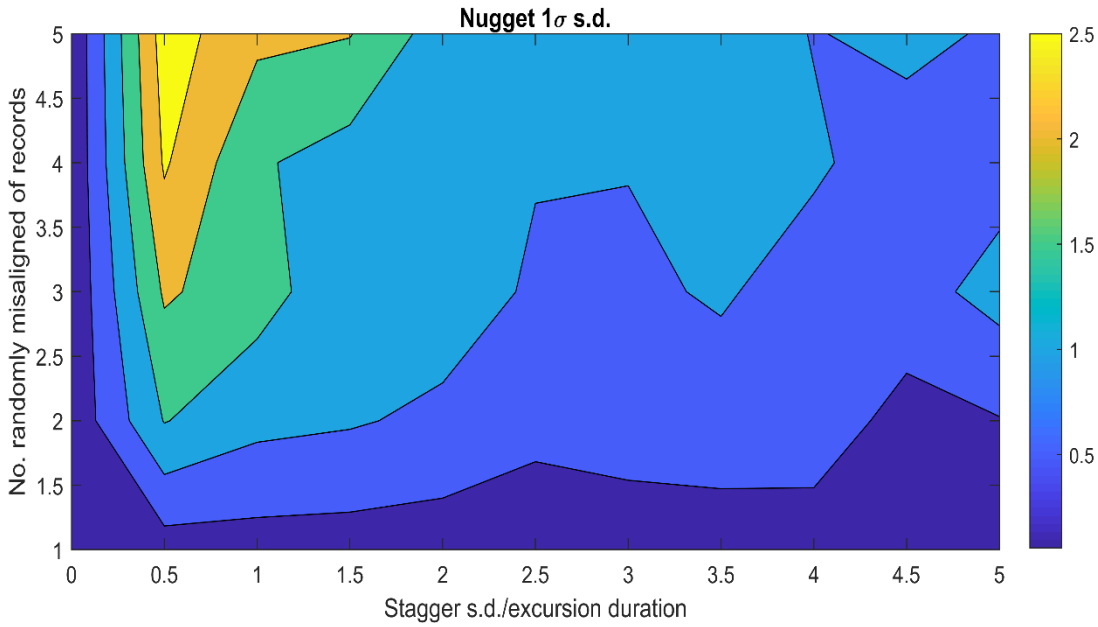

Supporting File d34S_Data.xlsx. *This Microsoft Excel spreadsheet contains all compiled $\delta^{34}S$ values, their assigned age, the proxy material from which they derive, and their source reference.*

Supporting Table S1. *Statistical description of all Phanerozoic $\delta^{34}S$ data. SD = standard deviation. CI = confidence interval.*

	n	mean	SD	median (95% CI)	skewness
Evaporite	1581	19.41	7.98	17.10 (16.76 – 17.44)	1.82
Biogenic CAS	912	18.87	5.14	18.80 (18.41 – 19.19)	0.28
Bulk CAS	3795	24.18	9.62	23.70 (23.38 – 24.02)	-0.48
Barite	422	19.50	2.22	19.15 (18.83 – 19.47)	-0.10
All data	*6710*	*22.04*	*8.79*	*21.08(20.86 – 21.30)*	*0.23*

Supporting Table S2. *References for $\delta^{34}S$ data included in compilation; number of CAS, evaporite, and barite analyses in each reference; and description of age assignments for the data.*

Reference	CAS	Evap.	Bar.	Age Model and Notes
Adams et al. (2010)	16			Ages linearly interpolated between Ar/Ar dates in provided in Figure 1 in paper. Stratigraphic heights extracted graphically.
Arp et al. (2008)	6			Assigned age of 146 Ma for the latest Tithonian
Ault & Kulp (1959)		12		Evaporite ages updated to latest stratigraphy. Omitted salt dome (migrated) samples from Feely & Kulp (1957), and only included samples with formation tabulated
Balderer et al. (1991)		11		Data compiled with age model by Bernasconi et al. (2017). Omitted vein and sandstone cement anhydrite samples.
Baldermann et al. (2015)	8			Linear interpoloation of stratigraphic height between Rb/Sr ages in paper
Bernasconi et al. (2017)		282		Age model provided in paper
Boschetti et al. (2011)		8		Data compiled with age model by Bernasconi et al. (2017)
Burdett et al. (1989)	56	25		Linear interpolation of stage boundaries from Berggren et al. (1985) to ICS2016/04 timescale. Ages and $\delta^{34}S$ extracted graphically from Figure 3.
Buschendorf et al. (1963)		24		Evaporites updated to latest stratigraphy. Omitted sulfide and barite samples.
Chen et al. (1981)		52		Translated from Chinese by Sang Chen, and $\delta^{34}S$ extracted graphically from figures. Only included Cambrian-Ordovician evaporites for which locality and unit could be determined.
Chen et al. (2013)	71			Linear interpolation of stratigraphic height between conodont zone age constraints from Kaufmann (2006), updated to GSSP ages in ICS2016/04
Claypool et al. (1980)		272		Evaporite ages updated to latest stratigraphy
Cortecci et al. (1981)		30		Used age model in Bernasconi et al. (2017), and assigned additional data from Western Alps to Rhaetian (Loprieno et al., 2011)
Dahl et al. (2019)	35			Ages provided in paper
Das et al. (1990)		6		Updated Michigan Basin chronostratigraphy from Rine et al. (2017)
Davies & Krouse (1975)		23		Evaporite ages updated to latest stratigraphy
Edwards et al. (2018)	117			Age model provided in paper
Fanlo & Ayora (1998)		26		Data compiled with age model by Bernasconi et al. (2017)
Fike & Grotzinger (2008)	157			Ages provided in Fike et al. (2015)
Fox & Videtich (1997)	13			Evaporite ages updated to latest Williston Basin stratigraphy using Taki & Pratt (2012)
Gill, Lyons, & Jenkyns (2011)	105			Linear interpolation of stratigraphic height between stage boundaries using ICS2016/04, assigning Calcari Maculati to Bajocian stage

Reference	CAS	Evap.	Bar.	Age Model and Notes
Gill, Lyons, Young, et al. (2011)	111			Linear interpolation of stratigraphic height between stage boundaries
Gill et al. (2007)	74			Linear interpolation of stratigraphic height between stage boundaries
Gomes et al. (2016)	115			Ages provided in paper on GTS2012 time scale, which matches ICS2016/04 in the Cretaceous
He et al. (2019)	165			Ages provided in paper for Siberian CAS data. For South China, age linearly interpolated by stratigraphic height between ICS2016/04 age of 529 Ma assigned to FAD of *W. crosby*i at base of Dahai Mbr, and age of 526.5 Ma to base of Shiyantou Fm. (Yang et al., 2018)
Hitchen & Krouse (1972)		6		Evaporite ages updated at stage scale to latest stratigraphy; omitted non-marine recent and migrated salt dome samples
Holser & Kaplan, Chem. Geol. (1966)		49		Evaporite ages updated to latest stratigraphy. Omitted salt dome (migrated) and secondary (cements/vugg-filling/intrusive igneous) textures
Horacek et al. (2010)		6		Data compiled with age model by Bernasconi et al. (2017)
Hovorka et al. (1993)		34		Assigned Delaware Basin ages from Wu et al. (2020) and Kerans and Tinker (1999). Data extracted graphically from Figure 5.
Hurtgen et al. (2009)	30			At Felix Cove, carbon isotope maxima in SPICE is set as base of Steptoean (Saltzman et al., 2004). In other sections, biomere event at onset of SPICE is set as base of Steptoean. March Pt. Formation includes *Bolaspidella* trilobites (Upper Middle Cambrian), and total deposition likely 5-10Ma; the lowest sample in the March Pt. Formation is set as the base of the Marjuman. Straigraphic heights extracted graphically.
Insalaco et al. (2006)		23		Age model provided by Bernasconi et al. (2017)
John et al. (2010)	34			Linear interpolation of stratigraphic height between conodont zone age constraints from Kaufmann (2006), updated to GSSP ages in ICS2016/04. Stratigraphic heights extracted from Fig. 4 and 5 graphically
Johnson et al. (2020)	130			Ages provided in paper interpolated to ICS2016/04
Jones & Fike (2013)	42			Linearly interpolated between stage boundaries using ICS2016/04. Hirnantian and Ordovician-Silurian boundary placed based on carbon isotope stratigraphy, not biostratigraphy, in text.
Kah et al. (2016)	42			Ages provided in Fig 9, using ICS2016/04 ages at the tie points
Kaiho et al. (2006)	11			Approximated age model as described for Schobben et al. (2017)
Kaiho et al. (2001)	12			Meishan section bed ages and accumulation rates from Burgess et al. (2014). Data tabulated in Kaiho et al. (2006)
Kaiho et al. (1999)	18			K-Pg boundary set at ICS2016/04 age, and sedimentation rates from paper. Data extracted graphically from Figure 3

Reference	CAS	Evap.	Bar.	Age Model and Notes
Kampschulte & Strauss (2004)	244			Ages updated by interpolation to ICS2016/04 from Harland 1989 Timescale (Harland et al., 1990). Data tabulated in Kampschulte (2001) and Kampschulte et al. (2001)
Kramm & Wedopohl (1991)		9		Zechstein evaporites tied to ICS2016/04 using ~1Myr/unit starting at the bottom of the Lopingian (Stollhofen et al., 2008)
Korte et al. (2004)	5			18.5m correlated by Gorjan & Kaiho (2007) to 250.7 Ma age in Bowring et al. (1998); linearly interpolated with *H. Parvus* FAD from Burgess et al. (2014)
Kozik et al. (2019)	48			Ages provided in paper in Fig. 3 based on Sr isotope stratigraphy by Saltzman et al. (2004)
Li et al. (2009)	27			Bed 27/28 boundary is proposed Permian-Triassic Boundary; using age from Burgess et al. (2014). Maokou/Wujiaping Fm. boundary is Guadalupian-Lopingian Boundary according to Yadong et al. (2008); using age from ICS2016/04. Data extracted from figures graphically.
Longinelli & Flora (2007)		8		Data compiled with age model by Bernasconi et al. (2017)
Loyd et al. (2012)	63			Linear interpolation of stratigraphic height between stage boundaries using ICS2016/04
Lu & Meyers (2003)		16		Middle Messinian age assigned in ICS2016/04
Luo et al. (2010)	58			Base of microbialite in Cili section correlated to base of Bed 25 in Meishan, and assigned age from Burgess et al. (2014); linearly interpolated height with FAD of *H. Parvus* assigned age from Burgess et al. (2014)
Lyu et al. (2019)	126			Ages provided in Fig. 8
Maharjan et al. (2018)	59			Linear interpolation of GTS2012 age model for conodont biostratigraphy provided in Fig. 1
Marenco et al. (2008)	25	9		Section correlated using flooding surfaces and Sr isotope data, and linearly interpolating ages of the Spathian/Anisian and Smithian/Spathian boundaries from Burgess et al. (2014)
Marenco et al. (2013)	20			Linear interpolation of stratigraphic height using stratigraphy published in Marenco et al. (2016), which uses ages in ICS2016/04. Data table appears truncated in publication; stratigraphic height and $\delta^{34}S$ extracted graphically from Fig. 4
Marenco et al. (2016)	7			Linear interpolation of stratigraphic height between stage boundaries in Fig 2, using ages from Kah et al. (2016), which match ICS2016/04
Meng, Zhang, Yan, et al. (2019)		5		Kept middle/upper Darriwilian assignment consistent with biostratigraphy and carbon isotope stratigraphy
Meng, Zhang, Schiffbauer, et al. (2019)		12		Tarim basin trilobite stratigraphy from Zhu et al. (2019). Includes one Lower Ordovician data from Cai et al. (2001) constrained to Tremadocian (Guo et al., 2018).
Mills et al. (2017)	114			Age model developed in paper on GTS2012 time scale, which matches ICSv2016/04 in the Cretaceous

Reference	CAS	Evap.	Bar.	Age Model and Notes
Newton et al. (2004)	32			Linear interpolation of stratigraphic height over the extinction interval using ages from Burgess et al. (2014), and age of 251.5 Ma for top of Tesero Ooilite set as the age at which the $\delta^{13}C$ returns to a "flat" value at the Meishan GSSP
Newton et al. (2011)	85			Linear interpolation of stratigraphic height between stage boundaries using ICS2016/04 for Yorkshire section, and correlated Tibet strata using chemostratigraphy preferred by the authors
Nielsen & Ricke (1964)		51		Evaporite ages updated to latest stratigraphy. Omitted caprock, stratigraphically unconstrained samples, lacustrine and freshwater-influenced samples, and Mg and K sulfates
Ohkouchi et al. (1999)	27			Age model based on Al accumulation provided in paper, and shifted +0.29 Myr to agree with ICS2016/04 Cenomanian-Turonian boundary age of 93.9Ma. Ages and $\delta^{34}S$ extracted graphically from Fig. 3A.
Owens et al. (2013)	216			Eastbourne section sedimentation rates between carbon isotope excursion features from Voigt et al. (2008) astrochronology tied to ICS2016/04 time scale using Cenomanian-Turonian GSSP. South Ferriby and Trunch sections tied to ages of CIE calculated for Eastbourne section and linearly interpolated stratigraphic height. Raia del Pedale section height linearly interpolated between CIE ages from Eastbourne and stage boundaries.
Pankina et al. (1975)		18		Evaporite ages updated to latest stratigraphy
Paytan et al. (1998)			69	Ages updated to ICS2016/04 from those provided in Kurtz et al. (2003), which uses Berggren et al. (1995) timescale. Ages for Sites 305, 366, and 577 updated to ICS2016/04 from those provided in Yao et al. (2020).
Paytan et al. (2004)			123	Ages updated to GTS2004 by Prokoph et al. (2008), and then interpolated to ICS2016/04
Peryt et al. (2010)		52		Evaporite ages updated to latest stratigraphy
Pisarchik & Golubchina (1975)		17		Evaporite ages updated to latest stratigraphy; omitted Vendian Motyi Formation
Playà et al. (2007)		10		Age of 70 kyr given in text
Posey & Fisher (1989)		59		Assigned Kungarian to lowermost Roadian age to reconcile top-Wolfcamp correlations between Midland and Palo Duro basins (Blomquist, 2016; Handford & Dutton, 1980; Mazzullo, 1982). Interpolated correlated wells as in Fig. 3
Poulton et al. (2015)	24			Sedimentation rates from Kolonic et al. (2005), rescaled to reflect obliquity-controlled cycles instead of eccentricity, as the authors prefer, citing Meyers et al. (2012). Cenomanian-Turonian boundary shifted from GTS2004 age in Kolonic et al. (2005) to ICS2016/04.
Present et al. (2015)	77			Ages determined by linearly interpolating stage boundaries, which are placed with carbon isotope stratigraphy as described by Jones & Fike (2013)

Reference	CAS	Evap.	Bar.	Age Model and Notes
Present (2018, Ch. 3)	52			ICS2016/04 ages used to interpolate biostratigraphy and carbon isotope stratigraphy in Bergström et al (2009) and Cramer et al. (2010)
Present et al. (2019)	255			Linearly interpolated stratigraphic height between high frequency sequence boundary ages in Wu et al. (2020)
Rennie & Turchyn (2014)	56			Site 807A to 362.8m: Martin & Scher (2004); Site 807A below 362.8m: Schrag et al. (1995); Site 821A: Wei & Gartner (1993); Site 1003A: Wright & Kroon (2000)
Rennie et al. (2018)	119			Age model provided in paper
Riccardi et al. (2006)	102			Used Burgess et al. (2014) ages for Meishan section and extinction interval at Shangsi, and for Dienerian base. Used Algeo et al. (2013) age for Changhsingian base. Used Bowring et al. (1998) age for base of Meishan bed #7.
Richardson et al. (2019)	93			Linearly interpolated ages with stratigraphic height given in Fig. 4
Rose et al. (2019)	118			Linearly interpolated stratigraphic height between Datum 2 bentonite age of 431.8 Ma and top of Sheinwoodian Sub-stage 2 from Cramer et al. (2012)
Sakai (1972)		13		Evaporite ages updated to latest stratigraphy. Omitted Precambrian samples, and samples purposely chosen to have anomalously-low $\delta^{34}S$
Schobben et al. (2015)	74			Ages provided in paper using Burgess et al. (2014) dates
Schobben et al. (2017)	19			Assigned approximate mid-Griesbachian age of 251.50 Ma to uppermost Balvany East strata, and linearly interpolated stratigraphic height to Permian-Triassic Boundary at base of Gerennavar Fm., neglecting missing section between Balvany East and Balvany North; used same accumulation rate for limestones in Nagyvisnyo Fm. anchored at EPME and apportioned remaining time in the Boundary Shale beds between top of limestones and P-Tr. Boundary
Schroder et al. (2004)		29		Ages provided in Fike et al. (2015)
Sim et al. (2015)	68			Ages provided in paper using Kaufmann (2006) time scale updated to GSSP ages in ICS2016/04
Solomon et al. (1971)		27		Evaporite ages updated at stage scale to latest stratigraphy
Song et al. (2014)	202			Age model is from Figure 4 (tie points are in bold), using dates from Burgess et al. (2014) and ICS2016/04; interpolated linearly in between tie points; Composite height is linking of sections by the C-isotope tie points in Figures 3 and 4: Daijang 400m = Lower Guandau 135m (N3); Lower Guandau 225m = Upper Guandau 10m (P4). Adjusted Daijang B by 18m to approx. bring in line with Daijang A, as in Fig 3

Reference	CAS	Evap.	Bar.	Age Model and Notes
Song et al. (2019)	29			Age model tied to Song et al. (2014) using correlation in Fig. 8 by linearly apportioning height between 40m and 48m to gap at Smithian-Spathian Boundary between 139.2m and 163m at Lower Guandau, and Burgess et al. (2014) age for base of Smithian at base of section
Spötl (1988)		8		German-language data compiled and assigned ages by Bernasconi et al. (2017)
Stebbins et al. (2019)	75			Age model provided in Supplemental Figure S4
Thode & Monster (1965)		68		Evaporite ages updated to latest stratigraphy. Data is reported as the range of measurements, so only could include the maximum and minimum values in compilation; omitted poorly-constrained intervals.
Thode & Monster (1970)		17		Evaporite ages updated at stage scale to latest stratigraphy
Thode et al. (1958)		5		Assigned to upper Frasnian (Hearn et al., 2011)
Thompson & Kah (2012)	235			Ages provided in paper using U/Pb dates in Thompson et al. (2012). Data tabulated in Thompson (2011).
Turchyn et al. (2009)	39		39	Ages updated by interpolation to ICS2016/04 from GTS2004
Utrilla et al. (1992)		62		Listed formations assigned by stage to ICS2016/04 ages. Omitted continental evaporite formations.
van Everdingen et al. (1982)		70		Evaporite ages updated to latest stratigraphy. Omitted vein gypsum.
Vinogradov (2007)		23		Toyonian evaporites assigned in 1 Myr intervals by subformation (Novikov, 2017)
Vredenburgh & Cheney (1971)		16		Evaporite ages updated to latest stratigraphy. Omitted "sulfur crusts."
Witts et al. (2018)	41			Linearly interpolated magnetochronological age assignments using stratigraphic heights.
Worden et al. (1997)		11		Used age model in Bernasconi et al. (2017)
Wotte et al. (2012)	85			Linear interpolation of stratigraphic height between stage boundaries
Wotte et al. (2011)	69			Linear interpolation of stratigraphic height between stage boundaries, using Susan Duster Limestone sedimentation rate for Molodo River and Ulakhan-Kyyry-Taas sections
Wu et al. (2014)	214		66	Ages updated by interpolation to ICS2016/04 from GTS2004. Data tabulated in Wu (2013).
Yan et al. (2013)	27			Guadalupian-Lopingian boundary set at base of *C.p.p.* based on ICS2016/04; Sedimentation rate from Qiu et al. (2015) indicate 0.04cm/kyr in the bedded chert relative to bentonite (257 Ma) at top of *C.p.p* zone, so base of bedded chert is 258.6 Ma.; applied this sed rate down through the limestone
Yao et al. (2018)			58	Age model provided in paper relative to PETM, which is taken as 55.93 Ma after Westerhold et al. (2008)
Yao et al. (2020)			88	Ages updated by interpolation to ICS2016/04 from GTS2012

Reference	CAS	Evap.	Bar.	Age Model and Notes
Yeremenko & Pankina (1972)		17		Evaporite ages updated to latest stratigraphy
Young et al. (2016)	68			Linear interpolation of stratigraphic height between stage boundaries in Fig 2 and 3
Young et al. (2019)	40			Assigned base and top of Ireviken CIE to bentonite age of 431.8 Ma and top of Sheinwoodian Sub-stage 2 (430.2 Ma) from Cramer et al. (2012) for Roberts Mtn. section. Aligned Newsom Roadcut carbon isotope record with Roberts Mtn. section, with unconformity on rising limb
Zhang et al. (2015)	15			Used Smithian/Spathian boundary ages from Burgess et al. (2014) and sedimentation rates provided in Figure 3